

1 Intermittent Bulk Release of Human Cytomegalovirus

2 Felix J. Flomm^{1,2,3,4}, Timothy K. Soh^{1,2,3,4}, Carola Schneider⁴, Linda Wedemann^{1,2,3,4}, Hannah M.
3 Britt⁵, Konstantinos Thalassinos^{5,6}, Søren Pfitzner⁴, Rudolph Reimer⁴, Kay Grünewald^{1,3,4,7}, Jens
4 B. Bosse^{1,2,3,4*}

5 ¹ Centre for Structural Systems Biology, Hamburg, Germany

6 ² Hannover Medical School, Institute of Virology, Hannover, Germany

7 ³ Cluster of Excellence RESIST (EXC 2155), Hannover Medical School, Hannover, Germany

8 ⁴ Leibniz-Institute for Experimental Virology (HPI), Hamburg, Germany

9 ⁵ Institute of Structural and Molecular Biology, Division of Biosciences, University College London,
10 London, United Kingdom

11 ⁶ Institute of Structural and Molecular Biology, Birkbeck College, University of London, London,
12 United Kingdom

13 ⁷ University of Hamburg, Department of Chemistry, Hamburg, Germany

14

15 *Jens B. Bosse, Center for Structural Systems Biology, Notkestraße 85, 22607 Hamburg

16

17 **Corresponding Author Email:** jens.bernhard.bosse@cssb-hamburg.de

18 Author ORCIDs

19 Felix J. Flomm: 0000-0001-7691-0519

20 Hannah M. Britt 0000-0001-8510-0331

21 Konstantinos Thalassinos 0000-0001-5072-8428

22 Søren Pfitzner 0000-0002-0155-0317

23 Kay Grünewald: 0000-0002-4788-2691

24 Jens B. Bosse: 0000-0001-7252-5541

25

26 Keywords

27 Human cytomegalovirus, Integrative microscopy, Viral egress, Morphogenesis

28

29 Author Contributions

30 Designed research: FJF, KT, RR, KG, JBB; Performed research: FJF, TKS, CS, LW, HB, RR;

31 Contributed new analytic tools: RR, CS, SP; Analyzed data: FJF, TKS, JBB; Wrote the paper:

32 KG, FJF, TKS, LW, JBB.

33

34 Abstract

35

36 Human Cytomegalovirus (HCMV) can infect a variety of cell types by using virions of varying
37 glycoprotein compositions. It is still unclear how this diversity is generated, but spatio-temporally
38 separated envelopment and egress pathways might play a role. So far, one egress pathway has
39 been described in which HCMV particles are individually enveloped into small vesicles and are

40 subsequently exocytosed continuously. However, some studies have also found enveloped virus
41 particles inside multivesicular structures but could not link them to productive egress or degradation
42 pathways.

43 We used a novel 3D-CLEM workflow allowing us to investigate these structures in HCMV
44 morphogenesis and egress at high spatio-temporal resolution. We found that multiple envelopment
45 events occurred at individual vesicles leading to multiviral bodies (MViBs), which subsequently
46 traversed the cytoplasm to release virions as intermittent bulk pulses at the plasma membrane to
47 form extracellular virus accumulations (EVAs). Our data support the existence of a novel *bona fide*
48 HCMV egress pathway, which opens the gate to evaluate divergent egress pathways in generating
49 virion diversity.

50

51 Introduction

52

53 Human Cytomegalovirus (HCMV) is a ubiquitous betaherpesvirus of high clinical importance that
54 establishes lifelong latent infection in humans. It is the leading cause of congenital disabilities in
55 the developed world and a significant cause of disease in immunocompromised patients, such as
56 transplant recipients, AIDS, or cancer patients (reviewed in [1]). HCMV has been ranked highest
57 priority for vaccine development by the Institute of Medicine for over 20 years [2]. Despite
58 continuing efforts, no approved vaccine exists so far, and antiviral therapy is currently the only
59 treatment option, with the development of viral resistance being a significant inherent concern [3].
60 As HCMV causes disease affecting various tissue types and organs, understanding how HCMV
61 can infect different cell types is essential for developing novel antiviral strategies.

62 HCMV infected cells release distinct virus populations that differ in their glycoprotein content [4,5]
63 to target specific cell types. While the pentameric complex consisting of
64 gH/gL/UL128/pUL130/pUL131 guides tropism for endothelial and epithelial cells, primarily through
65 cell-to-cell spread, the trimeric complex consisting of gH/gL/gO is needed to mediate infectivity of
66 cell-free virions. Factors that mediate the abundance of these complexes on virions have been
67 recently identified [5–9], but it is unclear how distinct glycoprotein concentrations on individual virus
68 particles are achieved. Spatio-temporally separated envelopment or egress pathways could explain
69 how distinct virus populations are generated, but little is known about these aspects during HCMV
70 assembly.

71 The virions of herpesviruses assemble in the host cytoplasm using a culminating step called
72 secondary envelopment. During secondary envelopment, viral capsids bud into host-derived
73 membranes, resulting in enveloped viral particles inside transport vesicles (reviewed in [10,11]).
74 These transport vesicles subsequently release mature virions by fusing with the plasma membrane.
75 Compared to the morphogenesis of the alphaherpesviruses Herpes simplex virus 1 (HSV-1) and
76 Pseudorabies virus (PRV), HCMV morphogenesis is much more involved, taking not only hours
77 but several days. During this time, the virus extensively remodels the host cell's secretory apparatus
78 leading to the formation of the assembly compartment (AC) [12]. The AC is a dense, donut-shaped,
79 perinuclear structure consisting of convoluted and interconnected membranes centered around the
80 microtubule-organizing center [13]. It contains many cellular proteins traditionally used as
81 organelle-specific markers, including proteins originally associated with Golgi, trans-Golgi,
82 endosomes, and lysosomes [14–17]. However, the extensive viral transformation of the cell's
83 secretory pathways during AC formation and the short-circuiting of established cellular pathways
84 through viral factors renders the origin of membranes and their identity less clear. Consistently,
85 proteomics analyses indicate that the virus-induced reorganization of the secretory apparatus
86 during AC formation leads to the mixing of membranes from different provenance as targets for
87 secondary envelopment [18].

88 Currently, secondary envelopment events have only been shown to occur as individual events at
89 small vesicles in the center of the AC [19,20]. This is consistent with data from alphaherpesviruses
90 where individual virions are continuously released through the fusion of diffraction-limited, virion-
91 containing exocytic vesicles with the plasma membrane [21,22]. In the case of HCMV, however,
92 studies also found enveloped particles in large multivesicular structures of unknown origin. These
93 large multivesicular structures, containing HCMV progeny, have been called endosomal cisternae

94 or multivesicular bodies (MVBs) in the literature, even though conclusive evidence regarding their
95 biogenesis has been lacking [14,23–25]. A recent study from the Wilson and Goodrum labs
96 suggested that virus-containing MVBs in HCMV fibroblasts and endothelial cells are derived from
97 membranes of different cellular origins [26].
98 Currently, it is unclear if virus particles in multivesicular structures represent a productive egress
99 pathway or are instead targeted for degradation since secondary envelopment at them or
100 subsequent release of virus progeny by exocytosis could not yet be demonstrated. Interestingly, it
101 has been shown that the deletion of the viral protein UL135 leads to an abrogation of virus-filled
102 MVB-like structures, and mutating UL71, a viral protein likely being involved in membrane scission
103 [27], led to an enlargement of these MVBs [24], possibly indicating their productive role. In addition,
104 a number of other publications implicate MVBs in HCMV morphogenesis [24,25,28–30], and data
105 from the related human herpesvirus 6A (HHV-6A) suggest MVB-like structures as targets for egress
106 [31].

107
108 To provide an unbiased view on HCMV envelopment and identify potential alternative HCMV
109 egress routes, we here employed an integrative approach based on volumetric live-cell imaging
110 and three-dimensional correlative light and electron microscopy (3D-CLEM). It provided an
111 unprecedented, spatio-temporally highly resolved view into whole HCMV infected fibroblast cells.
112 We found large transient accumulations of enveloped virions in MVB-like structures that were
113 positive for CD63 in line with previous reports. We dubbed these structures multi-viral bodies
114 (MViBs) as it is unclear at this point if their biogenesis parallels *bona fide* MVBs. Importantly, we
115 identified secondary envelopment events at MViBs, strongly suggesting that they are targets for
116 the viral envelopment machinery. Live-cell lattice light-sheet microscopy (LLSM) showed that
117 MViBs were transported to the plasma membrane, where they relaxed, and live-cell confocal
118 microscopy illustrated that these events lead to intermittent pulses of virus bulk release. Moreover,
119 a pH-sensitive biosensor functionally confirmed that the observed pulses were indeed due to
120 membrane fusion events. This intermittent virus bulk release led to the formation of extracellular
121 viral accumulations (EVAs) at the plasma membrane. Our data argue for a model in which a large
122 fraction of HCMV capsids envelope at MViBs, which subsequently are transported to the plasma
123 membrane where they fuse intermittently and release bulk pulses of viral particles. We propose
124 that this pathway likely constitutes a so-far neglected HCMV egress route. Future work is needed
125 to dissect its role in generating virion diversity.

126 127 **Results**

128 129 **HCMV-infected fibroblasts accumulate viral material at specific extracellular sites**

130
131 To get an overview of HCMV envelopment and egress routes, we initially used live-cell spinning-
132 disk fluorescence microscopy and followed the fate of capsids and viral membranes with an HCMV
133 mutant expressing EGFP-labeled capsid-associated tegument protein pp150 and mCherry-labeled
134 viral glycoprotein gM (HCMV-TB40-pp150-EGFP-gM-mCherry) [32] by single-particle tracking.
135 Despite considerable effort and computational filtering of thousands of analyzed capsid tracks, we
136 could not identify more than a few instances in which diffraction-limited capsid and membrane
137 signals merged and were subsequently co-transported. While we assumed that this was due to the
138 high signal background in the viral AC, it made us look for alternative HCMV egress and
139 envelopment routes that we missed by focusing on trackable small individual events.
140 Surprisingly, we found that between 72 and 96 hpi pp150-EGFP and gM-mCherry positive virus
141 material accumulated at defined sites in the extracellular space (Fig. 1).
142 These sites were reminiscent of exocytosis hotspots described for HSV-1 [33] (Fig. 1C) and we
143 dubbed them extracellular viral accumulations (EVAs). At 120 hpi, 80-90% of late-infected cells had
144 EVAs at their plasma membrane (Fig. 1B).
145 To investigate the nature and genesis of EVAs in HCMV-infected human foreskin fibroblasts, we
146 developed a novel three-dimensional correlative light and electron microscopy (3D-CLEM)
147 workflow that combines spinning-disk fluorescence microscopy with serial block-face scanning

148 electron microscopy (SBF-SEM). This approach allowed us to correlate specific labels for capsids
149 (pp150) and viral membranes (gM) with volumetric EM data of whole infected cells at high
150 resolution (Fig. 1D-E).

151 We identified EVAs below infected cells by fluorescence microscopy (Fig. 1C) and analyzed them
152 by 3D-CLEM (1D-F, Sup. Vid. 1). The EM workflow is based on aldehyde fixation, followed by an
153 adapted reduced-osmium, thiocarbonylhydrazide, osmium tetroxide (rOTO) regimen, as well as final
154 uranyl acetate and lead aspartate contrasting, which resulted in high contrast volumetric stacks
155 with well-defined membrane and capsid morphology. As depicted in Sup. Fig. 1, HCMV particles
156 in different stages of viral assembly could be clearly identified. DNA-filled virus capsids were easily
157 recognizable as dark contoured, round to hexagonal objects, with their condensed DNA visible as
158 a dark dot or a short line inside depending on orientation. We found that infected cells accumulated
159 virions, dark stained enveloped bodies, which likely represented dense bodies (capsid-free,
160 tegument only containing particles), and a plethora of vesicles of different sizes in pp150 and gM
161 positive EVAs (Fig. 1D-F). We also observed large invaginations at the plasma membrane that
162 might have resulted from either endo- or exocytosis of EVAs (two slices from a volume are shown
163 in Fig. 1F).

164

165 **HCMV particles bud into and accumulate in MVBs**

166

167 Next, we sought to investigate the source of EVAs. To our surprise, we found large intracellular
168 bodies positive for both capsid and viral membrane markers at four days post-infection (dpi). A z-
169 projection of a 3D spinning-disk microscopy stack from two adjacent cells is shown in Fig. 2B, and
170 a merge of these light and their respective EM data in Fig. 2C illustrates the correlation of the
171 datasets. Correlation of the large pp150 and gM positive spots identified in the fluorescent light
172 microscopy data with the respective EM volumes confirmed that they represented multivesicular
173 structures filled with significant numbers of virions, dense bodies as well as other structures (Fig.
174 2D,2F-G, Sup. Fig. 2, Sup. Vid. 2). To distinguish them from *bona fide* MVBs in the cell-biological
175 sense, we dubbed them multiviral bodies (MViBs). The MViBs in our data resembled structures
176 described in other studies [24,28], but it has been unclear if they result from a so-far unrecognized
177 egress pathway or a degradation pathway. To elucidate if MViBs could lead to EVAs, we quantified
178 their contents and compared the fractions of virions, dense bodies, and other vesicular material.
179 We found no significant difference between the content of the MViBs and EVAs (Fig. 2E),
180 supporting the hypothesis that EVAs are the result of MViB release. In general, MViBs were very
181 heterogeneous in size and content. Some contained only a few particles, others up to several
182 hundred; see also Sup. Fig. 3 for an overview of a complete AC and Sup. Vid. 3A-B for
183 representative whole-cell datasets. Sup. Vid. 2 depicts a representative MViB that we rendered and
184 where we segmented its contents and color-coded them as done in Fig. 2E. Importantly, we found
185 non-enveloped capsids on the surface of these MViBs (Sup. Vid. 4). Smaller virus-containing
186 vesicles described in previous EM-based studies [19] were often not as prominent in fluorescence
187 microscopy but could also be found in the SBF-SEM data (Sup. Fig. 4). We also regularly found
188 MViBs in cells infected with wild-type HCMV (Fig. 2H-I), confirming that MViBs are not an artifact
189 of the fluorescently-tagged mutants. We concluded that HCMV envelopment can lead to MViBs
190 and that EVAs had very similar contents.

191

192 **Pulses of bulk release lead to viral extracellular accumulations at the plasma membrane**

193

194 To illuminate the fate of MViBs, we used two live-cell fluorescence microscopy modalities. First, we
195 utilized inverted lattice light-sheet microscopy to acquire 3D volumes of infected cells at high
196 temporal resolution for 15-45 minutes for minimal phototoxicity and photobleaching. We found that
197 MViBs traveled from the assembly complex to the plasma membrane, where they seemed to relax,
198 possibly indicating their fusion with the plasma membrane (Fig. 3B, Sup. Vid. 5). In a second
199 approach, we imaged longer timespans in the infection cycle using time-lapse live-cell microscopy
200 with less temporal coverage in 2D. To this end, we used a modified HCMV mutant with more
201 photostable fluorescent tags (HCMV-TB40-pp150-SNAP-gM-mScarlet-I) for imaging z-stacks over

202 several days. We imaged HFF cells between 72 and 96 hpi for 18 to 60 hours every 40 minutes.
203 Strikingly, we observed MViBs coming close to the observation plane at the plasma membrane,
204 where they relaxed into patches of viral material (Fig 3C, Sup. Vid. 6-7). These patches were
205 identical in their phenotype to the EVAs shown in Fig. 1 and were positive for pp150 and gM. The
206 EVAs did not diffuse away but were often left behind when cells moved away, indicating that most
207 of the exocytosed material did not stay cell-associated. EVA formation generally occurred as
208 intermittent pulses as MViBs came into the observation plane near the plasma membrane and
209 relaxed (Sup. Vid. 6-7). The release events varied in their fluorescence intensity, consistent with
210 our observation that MViBs were very heterogeneous in size and content. Based on these
211 observations, we concluded that MViB exocytosis leads to EVA formation.

212

213 **MViBs release their cargo through fusion with the plasma membrane and result in EVAs**

214

215 To confirm that the observed bulk release events were indeed induced by fusion of MViBs with the
216 plasma membrane, we used the pH-sensitive fluorescent protein super-ecliptic pHluorin as a
217 biosensor to detect exocytosis events. We created a cell line stably expressing a CD63-pHluorin
218 fusion construct [34] as our data (presented in the next paragraph) indicated that CD63 is enriched
219 on MViBs membranes but not on virions. In this construct, pHluorin is inserted into an extracellular
220 loop of CD63, such that it points towards the luminal side in multivesicular structures and to the
221 extracellular environment after fusion. Accordingly, pHluorin is quenched by the acidic pH inside
222 this luminal space of MVBs, rendering the construct almost non-fluorescent. However, upon fusion
223 with the plasma membrane, pHluorin gets exposed to the pH-neutral extracellular milieu, and
224 fluorescence recovers rapidly. The increase in fluorescence intensity provides an easily detectable
225 and quantifiable indicator of fusion with the plasma membrane. Imaging of fixed, permeabilized
226 cells in which intracellular pHluorin was dequenched confirmed that the fluorescence signal from
227 the CD63-fusion marked gM and gB positive bodies (Sup. Fig. 5A-C, Sup. Vid. 8).

228 For imaging of potential fusion events, we picked cells that had not yet accumulated EVAs on the
229 outside of the basolateral cell surface and used live-cell total internal reflection microscopy (TIRF)
230 to image fusion events for several hours without phototoxicity. We took images every 1.5-2 seconds
231 for 60 minutes since we predicted that actual membrane fusion and pH equilibration might be very
232 rapid. We found that MViBs came into the TIRF-field and relaxed into EVAs shortly after arrival at
233 the plasma membrane. MViB fusion resulted in EVAs positive for pp150 and gM (Fig. 4B, arrows).
234 Quantification of the gM-mScarlet-I and pp150-SNAP signals showed that as the vesicular bodies
235 arrived at the plasma membrane, their fluorescence intensities increased until they peaked and
236 subsequently fell to stable plateaus of continuously elevated signals (Fig. 4C). Strikingly, these
237 events were accompanied by flashes of green fluorescence between the MViBs arrival and the
238 relaxation event, indicating that the membranes had fused (Fig. 4C). The reduction of green
239 fluorescence indicated that most of the CD63 diffused away from the fusion site. The gM and pp150
240 signals increased directly before the fusion event and decreased as MViBs relaxed into a flattened
241 patch. The exocytosed material emitted a continuously elevated signal. These results indicated that
242 MViB fusion with the plasma membrane led to EVA formation.

243

244

245 **MViBs carry markers of the endocytic trafficking system and the exosome pathway**

246

247 Intermittent bulk release of vesicles is a functional hallmark of exosomal pathways. Therefore, we
248 used immunofluorescence combined with mass spectrometry to approximate possible overlaps
249 between virus composition and exosome generation. To this end, we performed a mass
250 spectrometry analysis of gradient-purified extracellular virions. Gradient-purified virus particles
251 contained markers of Golgi-to-endosome trafficking (syntaxin 12, Rab14, VAMP3), early
252 endosomes (Rab 5C, syntaxin 7), as well as exosomes (HSP70, HSP90, GAPDH, enolase 1, 14-
253 3-3, and PKM2)[35], suggesting that HCMV might use a mix of membranes originating from Golgi-
254 and endosomal membranes for secondary envelopment to generate MViBs (Sup. Table 1, Sup.

255 Fig. 6). Our findings are consistent with a recent study, concluding that HCMV hijacks parts of the
256 exosome pathway for egress [36].
257 Other classical markers for membranes used in the exosomal pathway are the tetraspanins such
258 as CD9, CD63, and CD81. The role of CD63 in HCMV infection has been investigated before,
259 however, with conflicting results [37,38]. Using immunofluorescence, we tested if the tetraspanins
260 are localized to MViBs (Fig. 5A-C, Sup. Fig. 7A-B). The density of protein signals in the AC
261 complicated the analysis, yet we could identify CD63 colocalizing with large vesicles containing
262 pp150 and gM (Fig. 5A-C). We also performed EM with immunogold labeling against CD63 to
263 investigate its presence on MViBs at high spatial resolution. Although the content of large bodies
264 was often poorly retained after processing for immunogold staining, we regularly found HCMV
265 particles in large bodies that also were positive for CD63, indicated by the presence of nanogold
266 particles (Sup. Fig 8). However, CD9 and CD81, in our hands, localized to the AC but not
267 specifically to MViBs (Sup. Fig. 7A-B). Besides being present on the MViB limiting membrane,
268 exocytosed material in EVAs did not show any significant CD63 signal, implying that CD63 is
269 unlikely to be incorporated into virions (Fig. 5A-C). This observation is supported by the absence
270 of CD63 in our virion proteomics data (Sup. Tab. 1) and is in line with previous studies [39].
271 To gain further insight into the biological identity of MViBs, we tested if HCMV bulk release was
272 susceptible to inhibitors of MVB biogenesis or exosome release. Out of an initial panel of ten drugs
273 (Bexin-1, Simvastatin, Climbazole, GW4869, Ketotifen, Manumycin A, Nexinhib20, Suphisoxazole,
274 Tipifarnib, U18666A) that were described to influence MVB or exosome biogenesis, we
275 characterized the effect on HCMV for three of them (Ketotifen, Tipifarnib, U18666A) in more detail.
276 U18666A is an inhibitor of cholesterol trafficking [40,41], Tipifarnib is a farnesyl transferase inhibitor
277 with high activity against exosome production [42], and Ketotifen is a mast-cell stabilizing agent,
278 currently under investigation for its ability to block exosome release from cancer cells [43,44]. We
279 tested these drugs at concentration ranges between 0.1x and 2x of reported active concentrations
280 from the literature during virus infection. Only Tipifarnib was able to significantly reduce viral titers
281 at 4 dpi (Sup. Fig. 9C). Tipifarnib was also able to reduce the number of EVAs present at 5 dpi
282 (Sup. Fig. 9A-B, D). Moreover, we found no significant cytotoxicity of Tipifarnib in our HFF cells
283 compared to the vehicle control (Sup. Fig. 9E). While Tipifarnib had no pronounced effect on the
284 expression of the immediate-early genes IE1/2 or the early gene UL44, it had a significant effect
285 on the abundance of the late protein pp150, being a peripheral part of the viral capsid (Sup. Fig.
286 9F) in total cell lysates. Using Ketotifen, Tipifarnib, and U18666A, we were, therefore, unable to
287 delineate the biogenesis of MViBs.
288 While our data indicate a novel functional egress pathway for HCMV in which MViBs are targeted
289 for secondary envelopment and subsequently exocytosed, leading to the intermittent bulk release
290 of a large number of viral particles into EVAs, it is unclear at this point how MViBs relate to MVBs.
291 Future studies are needed, importantly also to illuminate the potential role of MViBs in releasing
292 virions of specific cell-tropism.

293 294 **Discussion**

295
296 Little data exist on the spatio-temporal organization of HCMV egress at the subcellular level.
297 Previous studies have mostly reported single-virion/single-vesicle envelopment events, which have
298 shaped our current picture of HCMV secondary envelopment [19,24]. These data are consistent
299 with a study by Hogue et al. [45], which shows that individual alphaherpesvirus virions are released
300 at the plasma membrane. Still, data suggests that virus-filled multivesicular structures can form in
301 HCMV-infected cells as well as HHV-6A and Murine Cytomegalovirus (MCMV) infected cells
302 [14,24,28,31,46] and that Golgi- and endosome-derived membranes are targeted by HCMV [14–
303 17,23,39]. While the previous literature often called these virus-containing multivesicular structures
304 "MVBs", we decided to dub them multi-viral bodies (MViB) as we could not untangle their descent
305 clearly. A recent study from the Wilson and Goodrum labs suggested that virus-containing
306 structures in HCMV fibroblasts and endothelial cells are derived from membranes of different
307 cellular origins [26]. Importantly, a functional role for these "virus-containing MVBs" or "MViBs" in
308 egress has lacked so far [14,23–25].

309

310 Here, we started by investigating EVAs. We were intrigued that most infected cells were positive
311 for EVAs late in infection and investigated their formation. Using a novel 3D-CLEM workflow that
312 combines dynamic information from spinning-disk fluorescence microscopy with high-resolution
313 information from serial block-face scanning electron microscopy, we found that HCMV can form
314 virus particles by budding into MViBs. By time-lapse and functional live cell imaging, we provide
315 evidence that MViBs can fuse with the plasma membrane and intermittently release tens to
316 hundreds of virus particles in bulk, resulting in plasma membrane-associated EVAs. Finally,
317 proteomics of purified virions, functional imaging, and correlation of CD63 localization with MViBs
318 suggested that MViB-mediated HCMV egress might use features of the cellular exosomal pathway;
319 however, drugs inhibiting MVB formation and exosome release showed no or inconclusive effects.

320

321 While EVAs represented static endpoints, MViBs were highly dynamic and transient. Integrating
322 imaging technologies that can cover large spatio-temporal ranges of HCMV infection proved to be
323 instrumental in analyzing the role of MViBs in HCMV egress. Our live-cell imaging indicates that
324 MViBs form relatively quickly between 72 and 96 hpi and are rapidly released asynchronously,
325 leading to pulses of EVA formation. This mechanism is in contrast to studies that have been
326 performed in alphaherpesviruses, where single PRV virus particles have been shown to travel to
327 the plasma membrane and be released by fusion [21]. Our data, however, does not exclude the
328 existence of a separate egress pathway, analog to the mechanisms shown for alphaherpesviruses
329 (reviewed in [47]). Compared to previous studies, our new correlative 3D-CLEM workflow provides
330 a major technological advancement permitting us to observe whole cells in a defined infection state
331 without the need for serial sectioning [19]. This has allowed us to analyze transient MViBs, which
332 would have been otherwise hard to catch at high resolution.

333 From our data, it remains unclear if HCMV uses *bona fide* cellular MVBs for envelopment and
334 transforms them into MViBs or if they are generated *de novo*. Cellular MVBs produce similar bulk
335 pulses of extracellular vesicles (EVs) or exosomes by fusion with the plasma membrane [48–50].
336 EVs form through budding into the lumen of late endosomes. This process generates MVBs
337 characterized by the presence of the late endosomal markers CD63, LAMP1, LAMP2, Rab4, and
338 Rab5 (reviewed in [50]). Budding at MVBs is catalyzed by the endosomal sorting complex required
339 for transport (ESCRT) [50]. While some parts of the ESCRT machinery play a role in the secondary
340 envelopment of alphaherpesviruses [27,51–53], they likely do not play a role in HCMV infection
341 [54–56]. However, it was recently shown that HSV-1 proteins pUL7 and pUL51 form a complex that
342 might constitute a mimic of an ESCRT-III complex. HCMV homologs pUL103 and pUL71 are
343 predicted to be structurally very similar to their HSV-1 counterparts and might likewise perform
344 ESCRT functions for the virus during infection [27]. A recent proteomics study supports this notion
345 by showing that HCMV utilizes parts of the exosome biogenesis machinery independently of
346 classical ESCRT-pathways [36].

347 Members of the tetraspanin family, such as CD9, CD81, and CD63, have also been described to
348 be enriched on EV membranes [48]. Tetraspanins are known to form microdomains called
349 tetraspanin-enriched microdomains on the cell surface [57] and are active in the organization of the
350 plasma membrane, recycling, and cellular signaling [57,58]. Tetraspanins are involved in sorting
351 and targeting cargo to MVBs and, in cooperation with the ESCRT machinery, into EVs [59,60].
352 While it has been shown that HCMV-infected cells release EVs that contain viral surface proteins
353 such as gB [61], the role of exosomal pathways in HCMV particle envelopment and release are
354 broadly not defined. Although inhibitors of exosome biogenesis can slow HCMV spread, they do
355 not significantly influence viral titers [37,62], possibly arguing for an involvement of the
356 MVB/exosome-pathways in cell-to-cell spread. Contradictory evidence exists for the role of CD63
357 in HCMV virus production. While one study did not find a significant effect of siRNA-mediated CD63
358 knock-down on HCMV titers [37], another recent study found a substantial reduction of HCMV titers
359 upon CD63 siRNA knock-down [38]. The reason for this discrepancy is difficult to determine since
360 the experimental settings in which each of the datasets was acquired varied drastically. This is
361 especially true for the virus strains used in these studies. While Hashimoto *et al.*, as well as Turner
362 *et al.*, used the lab-adapted AD169 strain, Streck *et al.* investigated the more clinical TB40/E strain

363 [36–38]. AD169 is adapted to release large amounts of supernatant virus from *in vitro* cultured
364 fibroblast, while strains like TB40/E, which resemble clinical isolates more closely, produce both
365 cell-associated virus and cell-free virus [63,64]. It is, therefore, tempting to speculate that release
366 pathways that rely on CD63 are used mainly by HCMV to produce cell-free virus, whereas other
367 pathways responsible for cell-associated spread might not be impaired in the absence of CD63.
368 We found colocalization between the tetraspanin CD63 and the viral envelope glycoproteins gB,
369 gM, and the tegument protein pp150. However, CD81 and CD9, which are also associated with
370 exosomes, did not colocalize with the viral markers as strongly. Since EVAs were negative for
371 CD63, this marker might be excluded during the budding process at the MVB surface. However,
372 this idea contradicts a previously published study showing that CD63 is incorporated in the virion
373 envelope [55]. Importantly, we and others did not find significant enrichment of CD63 in proteomic
374 analyses of purified HCMV virions [36]. CD63 possibly plays a role in the sorting of viral
375 glycoproteins to sites of secondary envelopment, as tetraspanins are known to be involved in
376 sorting plasma membrane-bound molecules into MVBs [59,60]. HCMV gB is known to localize to
377 the plasma membrane and be sorted through endocytic and recycling pathways by an acidic cluster
378 in its cytoplasmic domain [65,66]. For HSV-1, it was reported that disrupting the endosome-to-MVB
379 trafficking pathway leads to the mislocalization of HSV-1 gB [67]. More recently, it has also been
380 shown that HSV-1 replication leads to an increase in the exocytosis of CD63-containing
381 extracellular vesicles, leading the authors to hypothesize that HSV-1 modulates exosome
382 biogenesis for its benefit [68]. Taken together, these reports indicate that endocytic pathways can
383 be involved in the trafficking of viral factors to sites of herpesvirus secondary envelopment. Our
384 observation that HCMV gB strongly localized with CD63 might support this hypothesis and fits a
385 recent report that gB is enriched in exosomes [61]. Moreover, a recent proteomics study focusing
386 on exosome release from HCMV infected cells aligns with this interpretation [36]. This study further
387 identified several additional viral proteins that likewise appear in exosomes. The data provided by
388 the authors strengthen the overall idea that HCMV exploits endocytic trafficking and exosome
389 biogenesis pathways for the assembly and egress of virus particles. However, how much of the
390 host factors involved with exosome generation in the absence of virus infection are involved in virus
391 particle production remains unclear. In our hands, the MVB inhibitor U18666A does not influence
392 virus production. In contrast, Tipifarnib, an inhibitor of exosome biogenesis, significantly reduces
393 virus titers 4 dpi and EVA generation. Tipifarnib has been shown to reduce Rab27a, nSMase2, and
394 Alix levels, which might result in an effect on trafficking of viral components to assembly sites or
395 membrane remodeling during secondary envelopment [42]. Alternatively, inhibition of the cellular
396 farnesyltransferase by Tipifarnib might also act on Ras signaling pathways, which have been
397 reported to positively influence HCMV, HSV-1, and other herpesvirus infections [69–71]. An effect
398 of Tipifarnib on transcription would be the simplest explanation for the reduced pp150 levels at 3
399 and 4 dpi. On the other hand, inhibition of downstream HCMV assembly processes might also
400 result in the degradation of structural proteins such as pp150. Moreover, it is conceivable that the
401 host farnesyltransferase is directly involved in the post-translational modification of virus proteins
402 and that its inhibition by Tipifarnib has a negative effect on viral protein levels and replication.
403 Instead of being the result of an altered MVB pathway, MViBs might originate from the fusion of
404 individual virus-filled transport vesicles as described for the related betaherpesvirus HHV-6A [31].
405 This model fits reports that MViBs were mostly found in the AC periphery while most capsid budding
406 into individual vesicles is observed in the center of the AC, where early endosomal markers and
407 Golgi-markers merge [15,16]. However, in the work we present here, we regularly found budding
408 events at MViBs but could not identify intracellular vesicle fusion events leading to MViB formation
409 in entire 3D-EM volumes of infected cells. We, therefore, conclude that MViB-mediated HCMV
410 egress is a novel spatio-temporally separated egress pathway.
411 HCMV produces cell-free virus in addition to cell-associated virus in fibroblasts and predominantly
412 cell-associated progeny in endothelial cells [4]. These different particle populations vary in their
413 trimeric to pentameric glycoprotein complex composition, resulting in their different cell tropism. It
414 is plausible to hypothesize that these virus populations might undergo different envelopment
415 processes in the cell and are exocytosed with a different spatio-temporal profile [4]. A recent study
416 from the Wilson and Goodrum labs suggests that virus-containing MVBs in fibroblasts and

417 endothelial cells are derived from different cellular membranes, which would add another potential
418 HCMV egress pathway that could result in different virus populations; however, it is unclear if these
419 pathways are functional in egress [26].

420 Future work needs to focus on characterizing the particle populations exocytosed by these different
421 pathways regarding their glycoprotein content and define their role in potentially divergent egress
422 routes. We used the HCMV strain TB40, which can produce two virus populations on HFF cells
423 which are endothelial-cell and fibroblast-topic [4]. The EVAs that we found were largely static during
424 live-cell imaging and might represent a cell-associated viral population. We found EVAs not only
425 trapped between the cell and the cell support but also on the upper side of infected cells, as well
426 as between cells. This observation would support the idea of cell-to-cell spread. However, our
427 proteomics data and a recent study [36] found that soluble, purified virions showed markers of the
428 exosome pathway. If the virions released through EVAs are the only ones that carry exosome-
429 markers, this would suggest that it is unlikely that they stay cell-associated and play a role in cell-
430 to-cell spread.

431 In summary, our data, combined with published studies, suggest a model in which membranes
432 originating from a fusion of both the endosomal and trans-Golgi network are used for either
433 individual envelopment of capsids or to generate MViBs in two spatio-temporally separated
434 processes. MViBs are then transported to the plasma membrane, where fusion results in bulk
435 pulses of virus particle exocytosis and the formation of EVAs (Fig. 6). Future work is needed to
436 delineate the biogenesis of MViBs and, importantly, their potential role in producing specific virus
437 populations.

438

439 **Materials and Methods**

440

441 **Cells and Viruses**

442

443 HFF-1 cells (ATCC-SCRC-1041, ATCC) were cultivated in Dulbecco's Modified Eagles Medium
444 Glutamax (Thermo Fisher Scientific), supplemented with 5% FBS superior (Merck) and 2×10^5
445 units/ml Recombinant Human FGF-basic (PeproTech Inc.). HCMV-pp150-EGFP-gM-mCherry was
446 a kind gift by Christian Sinzger [32]. The HCMV-TB-40-BAC4 was a kind gift by Wolfram Brune
447 [72]. Different multiplicities of infection (MOIs) were used for the infection experiments. In general,
448 low MOI infections were used to avoid artifacts generated by high virus doses. Therefore, whenever
449 possible, we used MOIs between 0.5 and 1. However, for particular experiments, such as bulk
450 assays or electron microscopy, we used MOIs of up to 5. The used MOI is indicated for each
451 experiment.

452

453 **Spinning-disk Fluorescence Microscopy**

454

455 Spinning-disk microscopy was carried out on a Nikon TI2 (Nikon) based spinning-disk system
456 equipped with a Yokogawa W2, a Nikon 1.49 NA Apo-TIRF objective, and an Andor iXON888
457 EMCCD (Andor Technology). The resulting pixel size was 130nm, and image acquisition was done
458 with NIS-Elements. Further, the setup was equipped with 405, 488, 561, and 640 laser lines and
459 corresponding filter sets. Life cell experiments were carried out with a humidified incubation
460 chamber heated to 37°C and 5% CO₂ controlled by a gas mixer. For fluorescence microscopy,
461 cells were grown in Ibidi 35mm glass-bottom dishes (Ibidi GmbH), for CLEM in Ibidi 35mm grid
462 polymer bottom dishes. SNAP labeling before live-cell imaging with SNAP-Cell 647-SIR (New
463 England Biolabs GmbH) was done according to the manufacturer's instructions. Image processing
464 and analysis were performed in ImageJ/FIJI.

465

466 **Serial Block Face Scanning Electron Microscopy (SBF-SEM)**

467

468 For SBF-SEM, cells were fixed at the indicated time-points with 2% Paraformaldehyde (PFA/
469 Science Services) and 2.5% Glutaraldehyde (GA/ Science Services GmbH) in Dulbecco's
470 phosphate-buffered saline (D-PBS, Sigma-Aldrich) for 5 minutes at room temperature (RT) and 55

471 minutes on ice. Subsequently, the sample was processed with the following procedure: Postfixation
472 with 2% Osmium Tetroxide (OsO₄/ Science Services) and 2.5% GA in D-PBS on ice, staining with
473 2% OsO₄, 1.5% potassium ferrocyanide (Sigma-Aldrich), 2mM CaCl₂ (Sigma-Aldrich) in water,
474 incubation in 0.5% thiocarbohydrazide (Sigma-Aldrich) in water, staining with 2% OsO₄ in water,
475 incubation in 1% gallic acid (Sigma-Aldrich) in water, staining with 2% uranyl acetate (Merck KGaA)
476 overnight in water. On the next day, the sample was stained with freshly prepared Waltons lead
477 aspartate [73] (Pb(NO₃)₂ (Carl-Roth), L-Aspartate (Carl-Roth), KOH (Merck)), and subsequently
478 subjected to a PLT dehydration series to Ethanol Rotipuran (Carl-Roth). Finally, the samples were
479 infiltrated with 70% Epon in Ethanol before two incubations with 100% Epon and the final
480 polymerization was carried out in Epon supplemented with 3% silver flakes (Sigma-Aldrich) and
481 3% (w/w) Ketjen Black (TAAB). Sample blocks of 0.5x0.5 mm were cut, mounted, and inserted into
482 a Gatan 3View stage (Gatan) built in a Jeol JSM-7100F scanning electron microscope (Jeol). For
483 imaging, the sample stage was biased with a 500V positive charge to account for sample charging
484 during the scanning process. For the acquisition, 3x3 nm pixel size images were scanned, followed
485 by the repeated ablation of 50 nm sections. The acquisition was controlled by the Gatan Digital
486 Micrograph software, which was also used for stack alignments. Further processing of the datasets
487 was performed in FIJI, and the volumes were rendered in Imaris 8 (Bitplane). To quantify MViB and
488 EVA compositions, subvolumes of those structures were randomly chosen and extracted.
489 Subsequently, particles were manually identified and counted. The image handling tasks were
490 performed in ImageJ/FIJI. Statistical analysis was performed in GraphPad Prism 8.

491

492 **Transmission Electron Microscopy (TEM)**

493

494 For TEM, cells were fixed and processed as described for SBF-SEM up to the embedding step.
495 The cells were embedded in Epon without fillers, sectioned to 50 nm on a Leica Ultracut Microtome
496 (Leica), and transferred to copper mesh grids. Electron microscopy was performed on an FEI
497 Tecnai G20 (FEI/ Thermo Fisher Scientific), and images were acquired on an Olympus Veleta side-
498 mounted camera (Olympus).

499

500 **Lattice Light Sheet Microscopy**

501

502 Lattice light-sheet microscopy was performed on a Zeiss Lattice Light Sheet 7 (Carl Zeiss) as part
503 of an early adaptor program, controlled with Zeiss Zen Blue software. The device is equipped with
504 488, 561, and 640 laser lines and multi-bandpass filters. Live-cell experiments were carried out on
505 Ibidi 35mm glass-bottom dishes at 37°C with 5% CO₂ in a humidified atmosphere. Images were
506 acquired on a pco.edge (PCO AG) sCMOS camera with a final pixel size of 145nm. Images were
507 deconvolved after acquisition in Zen Blue using the built-in constrained-iterative algorithm. 2D
508 image processing was done in Zen Blue, arrangements and montages were made in FIJI. 3D image
509 processing was done in Arivis 4D (arivis AG); videos were cut and arranged in Adobe Premiere
510 Pro (Adobe Inc).

511

512 **BAC Mutagenesis**

513

514 BAC mutagenesis was performed as described before by en-passant Red Recombination [74]. The
515 creation of HCMV-TB40/BAC4-pp150-SNAP-gM-mScarlet-I was done in two steps. At first, UL32
516 (gene locus of pp150) was mutated by the C-terminal insertion (after K1045) of the SNAP-Tag-
517 SCE-I-KanR shuttle sequence with a nine amino acid linker (HTEDPPVAT) and subsequent second
518 recombination to clear the Kanamycin resistance and restore the SNAP-Tag sequence (NEB; for
519 complete insertion sequence see Table 1). This was followed by the insertion of the mScarlet-I [75]
520 sequence in the UL100 gene between the codons for amino acids V62 and M63 of gM by amplifying
521 the mScarlet-I-SCE-I-KanR shuttle construct with the primers shown in Table 2, with the second
522 recombination as described for the first step. The virus was reconstituted by electroporation of the
523 BAC DNA into HFF cells.

524

525

526 **Gateway Cloning and Lentivirus Transduction**

527

528 Plasmid pCMV-Sport6-CD63pHluorin was a gift from DM Pegtel through Addgene (Addgene
529 plasmid # 130601 ; <http://n2t.net/addgene:130901> ; RRID:Addgene_130901, Addgene). For
530 Gateway (Thermo Fisher Scientific) cloning, the pCMV-Sport6-CD63pHluorin was recombined with
531 pDONR-221 (Thermo Fisher Scientific) to produce the pENTR-CD63pHluorin vector that was
532 further recombined with pLenti-CMV-Puro-DEST (w118-1), a gift from Eric Campeau & Paul
533 Kaufman through Addgene (Addgene plasmid # 17452; <http://n2t.net/addgene:17452>; RRID:
534 Addgene_17452).

535 The resulting pLenti-CMV-CD63pHluorin-Puro was then transfected with polyethyleneimine
536 (Polysciences) together with 3rd generation Lentivirus vector helper plasmids, gifts by Didier Trono,
537 RRID: Addgene_12253, Addgene_12251, Addgene_12259) into 293XT cells (Takara Holdings).
538 Lentivirus containing supernatant was harvested at 48, 72, and 96 hours post-transfection, filtered
539 through 0.2 µm syringe filters, and used to transduce HFF-1 cells. 72hpi, the HFF-cells were
540 selected with Puromycin (Thermo Fisher Scientific) at 5 µg/ml. Furthermore, the cells were sorted
541 by fluorescence-activation (FACS), using a FACS Aria Fusion (BD Biosciences), for the 10%
542 strongest fluorescent cells, further cultivated and used for the experiments.

543

544 **Immunofluorescence**

545

546 For immunofluorescence experiments, cells were grown in 35mm glass-bottom Ibidi dishes and
547 fixed at the indicated time-points with 4%PFA in D-PBS. SNAP labeling with SNAP-Cell 647-SIR
548 was done as described in the manual for SNAP-Cell 647-SIR (NEB). Afterward, the samples were
549 permeabilized with TritonX-100 at 0.1% in D-PBS with subsequent blocking with 3% Bovine Serum
550 Albumin (Sigma-Aldrich) in D-PBS. Primary antibodies used in this study were Ultra-LEAF™
551 Purified anti-human CD63 H5C6 (Biolegend), Anti-Cytomegalovirus Glycoprotein B antibody [2F12]
552 (ab6499) (Abcam), Purified anti-human CD9 HI9a (Biolegend), Purified anti-human CD81 (TAPA-
553 1) 5A6 (Biolegend). Secondary antibodies used were Alexa 647 goat anti-mouse (Thermo Fisher
554 Scientific) and Alexa 488 goat anti-mouse (Thermo Fisher Scientific).

555

556 **Quantification of the frequency of extracellular viral assemblies**

557

558 HFF-WT cells were infected with HCMV-pp150-SNAP-gM-mScarlet-I or HCMV-TB40-WT at an
559 MOI of 1 and fixed at 120hpi. HCMV-TB40-WT infected cells were stained for gB as described for
560 the other immunofluorescence experiments. Late infected cells were identified in WT-infected cells
561 by a well identifiable gB-positive assembly complex. In the HCMV-pp150-SNAP-gM-mScarlet-I
562 infected cells, late infected cells were identified by three conditions: 1) Well identifiable gM-positive
563 assembly complex. 2) Nuclear signal of pp150-SNAP. 3) Significant pp150-SNAP signal in the
564 assembly complex.

565 **Confocal Scanning Imaging**

566

567 Confocal Laser Scanning Microscopy was carried out on a Nikon T12 microscope equipped with an
568 A1 confocal laser scanning unit, a 1.4 NA 60x Plan Apo objective, PMT, and GaAsP detectors,
569 standard 404, 489, 561, and 637 laser lines, and corresponding filter sets (Nikon). Imaging
570 conditions were optimized for each sample. Scan sizes were adapted to fulfill the criteria for
571 Nyquist-sampling, resulting in a pixel size of 118 nm. The acquisition was run in NIS-Elements,
572 post-processing and image analysis were performed in FIJI.

573

574 **Weighted Spatial Colocalization Analysis**

575

576 For the weighted colocalization heatmaps, pixel intensities were calculated, taking into account the
577 absolute intensities in both channels and the ratio between the intensities. The calculation was

578 performed by first normalizing each channel to relative intensity. In the following, the relative
579 intensities of each pixel in both channels a and b were interpreted as a vector $\begin{pmatrix} a \\ b \end{pmatrix}$ Describing the
580 vector to the position of that pixel in a classical scatter plot. The length of the vector was then
581 multiplied by $1 - |\sin(\alpha) - \cos(\alpha)|$ while α is the angle between the vector and the x-axis. This
582 multiplication emphasizes pixels where the two colors colocalize with similar relative intensities.
583 The product then was plotted back to the original pixel position in the image resulting in the heatmap
584 shown in the figures. With this strategy, we could put the information of a 2-channel scatter plot
585 back into the image's spatial context.
586 The Jupyter notebook for this analysis is available on GitHub:
587 (<https://github.com/QuantitativeVirology/2D-Colocalization>)
588

589 **Gradient purification of HCMV**

590
591 A 15 cm dish of HFF cells was infected with HCMV-TB40-WT at MOI 0.05. Seven dpi, the infected
592 cells were trypsinized and split onto 16x 15 cm dishes of HFF cells. 7 days after subculturing, the
593 supernatant was harvested and clarified by centrifugation at 1200 xg for 5 min. The virus was
594 pelleted by centrifugation at 14000xg for 1.5 h at 4°C and then resuspended in 1% FBS/PBS
595 overnight on ice. The resuspended virus was centrifuged at 18000xg for 1 min at 4°C to remove
596 large aggregates and then loaded over a continuous gradient made from 15% sodium tartrate with
597 30% glycerol (w/w) and 35% sodium tartrate (w/w) in 40 mM sodium phosphate pH 7.4 [76]. The
598 gradient was made with a Gradient Master (BioComp Instruments) for an SW41 rotor. After
599 centrifugation at 65000xg for 1.5 h at 4°C, the bands were isolated, diluted 10-fold in PBS, and
600 pelleted at 14000xg for 1.5 h at 4°C. The purified virus pellet was resuspended overnight in PBS
601 and stored at -80°C.
602

603 **Mass Spectrometry**

604
605 The purified virus was mixed with 3 volumes of lysis buffer (100 mM Tris, 50 mM DTT, 8 M Urea
606 pH 8.5) and incubated at room temperature for 15 min. Samples were digested using the FASP
607 protocol, employing 30 kDa molecular weight cut-off filter centrifugal units (Amicon, Merck, [77]).
608 Briefly, the lysed virus was added to the centrifugal unit and washed with TU buffer (100 mM Tris,
609 8 M Urea pH 8.5). Next, 8 mM DTT in TU buffer was added and incubated at 56°C for 15 min. After
610 two further washes, 50 mM iodoacetamide (IAA) in TU buffer was added and incubated for 10
611 minutes at room temperature. The centrifugal units were washed twice, treated again with DTT,
612 washed once further with TU buffer, and twice with 50 mM ammonium bicarbonate solution. MS
613 grade trypsin (Promega) was added in a 1:100 enzyme:protein ratio, and the sample was incubated
614 overnight at 37°C. The flow-through containing trypsinized peptides was collected and pooled, and
615 the sample was lyophilized with a SpeedVac (Thermo Fisher Scientific). The resulting peptides
616 were enriched with C18 stage tips prepared in-house and eluted with 80% acetonitrile containing
617 0.5% acetic acid. The samples were dried down by SpeedVac (Thermo Fisher Scientific) and
618 resuspended in 97% water, 3% acetonitrile with 0.1% formic acid, and 10 fmol/ μ L E. coli digest
619 (Waters Corporation) for analysis by LC-MS/MS.
620

621 Peptides resulting from trypsinization were analyzed on a Synapt G2-Si QToF mass spectrometer
622 connected to a NanoAcquity Ultra Performance UPLC system (both Waters Corporation). The data
623 acquisition mode used was mobility enhanced MSE over m/z range 50-2000 with the high energy
624 collisional voltage in the transfer region ramped from 25 to 55 V. Mobile phases used for
625 chromatographic separation were water with 0.1% formic acid (A) and acetonitrile with 0.1% formic
626 acid (B). Samples were desalted using a reverse-phase SYMMETRY C18 trap column (100 Å, 5
627 μ m, 180 μ m x 20 mm, Waters Corporation) at a flow rate of 8 μ l/min for 2 minutes. Peptides were
628 separated by a linear gradient (0.3 μ l/min, 35 °C; 97-60% mobile phase A over 90 minutes) using
629 an Acquity UPLC M-Class Reversed-Phase (1.7 μ m Spherical Hybrid, 76 μ m x 250 mm, Waters
630 Corporation).

631

632 LC-MS data were peak detected and aligned by Progenesis QI for proteomics (Waters
633 Corporation). Proteins were identified by searching against the Human and HCMV proteomes in
634 Uniprot. The database search was performed with the following parameters: mass tolerance was
635 set to software automatic values; enzyme specified as trypsin; up to two missed cleavages;
636 cysteine carbamidomethylation as a fixed modification, with the oxidation of methionine, S/T
637 phosphorylation, and N-terminal acetylation set as variable modifications. Abundances were
638 estimated by Hi3-based quantitation [78].

639 For comparison with the Turner et al. (2020; [36]) dataset, protein accession was converted to
640 UniParc codes. Raw MS data have been deposited to PRIDE with accession code PXD023444.

641

642 **Live TIRF Microscopy**

643

644 For live-cell TIRF imaging, infection experiments were carried out in 35 mm glass-bottom Ibidi
645 dishes. SNAP labeling with SNAP-Cell 647-SIR was done as described in the manual for SNAP-
646 Cell 647-SIR (NEB) before imaging. Microscopy was performed on a Nikon TI equipped for TIRF
647 microscopy and equipped with standard 488, 561, and 640 laser lines, corresponding filter sets,
648 and an incubation chamber with a heating system. The illumination angle was determined
649 experimentally by manually adjusting for TIRF illumination, and image acquisition was performed
650 with NIS-Elements using an ANDOR iXon Ultra 897 EMCCD camera. Live-cell experiments were
651 carried out at 37°C. Intensity measurements in the time courses were done with FIJI by manually
652 placing ROIs. The data analysis and visualization in the graphs were performed in GraphPad Prism
653 8.

654

655 **Immunogold labeling**

656

657 For immunogold labeling of HCMV infected cells, 1x 10 cm cell culture dish of HFF-WT cells were
658 infected with HCMV-WT at an MOI of 0.5. At 4 dpi, the cells were fixed with a mixture of 2% PFA
659 and 0.5% GA (both Science Services) in PBS (Sigma-Aldrich) for 10 minutes at 37°C and 5% CO₂.
660 The cells were washed once in PBS and subsequently scraped in 1% gelatin (food grade brand).
661 The cells were pelleted, resuspended in 10% gelatin, and pelleted again while letting the gelatin
662 cool to solidify. The gelatin with the embedded cell pellet was cut into small (1-3 mm) chunks,
663 immersed in 2.3M Sucrose solution, and stored overnight at 4°C. The next day, the pieces were
664 mounted on a sample holder and flash-frozen by immersion in liquid nitrogen. Afterward, the pieces
665 were trimmed and sliced into 70 nm thin sections on a Leica EM FC7 cryo-microtome (Leica) using
666 a diamond knife (Diatome). The sections were recovered by picking them up with a drop of 2.3M
667 Sucrose and transferring them to Formvar and carbon-coated nickel grids, letting the sections thaw
668 in the process. In the following, the sections were immunogold labeled by the following protocol:
669 removal of residual gelatin by incubation in PBS for 20 minutes at 40°C. 3x 2 minutes incubation
670 with PBS, 3x 2 minutes incubation in 0.1% Glycine (Sigma-Aldrich) in PBS, and blocking for 3
671 minutes in Aurion donkey serum (Aurion/ Science Services). After blocking, the samples were
672 incubated with Ultra-LEAF™ Purified anti-human CD63 H5C6 antibody (Biolegend), diluted 1:5 in
673 Aurion donkey serum, for 30 minutes. Afterward, the samples were washed 5x 2 minutes in PBS
674 and incubated with 10 nm gold coupled donkey-anti-mouse IgG (Aurion/ Science Services), diluted
675 1:20 in Aurion donkey serum, for 1 hour. Subsequently, the samples were washed 5x 2 minutes in
676 PBS, followed by fixation with 1% GA in PBS for 5 minutes. Afterward, the samples were incubated
677 10x 1 minute in distilled water and stained, first with uranyl acetate (Merck) in water and secondly
678 with uranyl acetate in 1% methylcellulose. Finally, the grids were air-dried after blotting the uranyl
679 acetate-methylcellulose solution and observed by transmission electron microscopy.

680

681 **Inhibitor Treatments**

682

683 U18666A was acquired from Merck, Ketotifen-fumarate, and Tipifarnib were bought from Sigma-
684 Aldrich. The substances were dissolved in DMSO to produce stock solutions (U18666A at 4 mg/ml,

685 Ketotifen at 20 mM, and Tipifarnib at 5 mM), which were subsequently aliquoted and frozen at -
686 80°C. The drugs were added to the complete growth medium at the indicated time points and at
687 the concentration indicated for each experiment. The medium containing the inhibitor was renewed
688 every 24 hours.

689

690 **Titration**

691

692 To assess the virus titers in supernatant from HCMV infected cells. HFF-WT cells were seeded in
693 24-well dishes to reach 90-100% on the next day. Tenfold dilutions of the harvested infectious
694 supernatants were made in complete growth medium from 10^{-1} – 10^{-4} . The medium from the HFF
695 cells was removed and replaced by 100 μ l of one of the dilutions per well. The plates were rocked
696 gently every 15 minutes for 1 hour to ensure even distribution. After one hour of incubation, an
697 overlay of DMEM containing 2% FCS and 0.6% Methylcellulose (Sigma-Aldrich) was added to the
698 cells, and the plates were incubated at 37°C and 5% CO₂ for 14 days. Afterward, the cells were
699 fixed, and fluorescent virus plaques were counted.

700

701 **Cytotoxicity Assays**

702

703

704 HFF-WT cells were seeded on a black 96-well plate to reach confluency on the next day. Then the
705 cells were treated with the indicated substance and concentration for 24 hours. Afterward, the cell
706 viability was measured using the CellTiter-Glo® luminescent cell viability assay (Promega) and a
707 FLUOStar Omega plate reader (BGM Labtech), both according to the instructions from the
708 manufacturer.

709

710

711 **Western Blotting**

712

713 HFF-WT cells were infected with HCMV-WT (MOI = 3), cells were harvested and lysed at 1 hpi
714 (input) and every 24 hours until 96 hpi. SDS-PAGE was performed on Bio-Rad Mini-PROTEAN
715 TGX 4-15% gels (Bio-Rad). Separated protein was blotted on Amersham Protran 0.45 μ m
716 nitrocellulose membranes (Cytiva). The membrane was cut, and the sections were subsequently
717 stained with one of the primary antibodies against HCMV pp150 (kind gift by Eva-Maria Borst and
718 Stipan Jonjic), anti-CMV ICP36 monoclonal antibody 10D8 (Virusys), and anti-IE1/2 (hybridoma
719 supernatant [79], kind gift by Wolfram Brune) followed by a secondary antibody Goat Anti-Mouse
720 IgG StarBright Blue 700 (Bio-Rad). The stained blots were imaged using a ChemiDoc MP imager
721 (Bio-Rad).

722

723

724 **Acknowledgments**

725

726 We thank Wolfram Brune, Christian Sinzger, and Kerstin Sampaio for their generous gift of viruses
727 HCMV-TB-40-BAC4, HCMV-pp150-EGFP-gM-mCherry, reagents, and their support.

728

729 This study was funded by the Wellcome Trust through a Collaborative Award (209250/Z/17/Z) to
730 KT, KG, and JBB. KG and JBB are funded by the Deutsche Forschungsgemeinschaft (DFG,
731 German Research Foundation) under Germany's Excellence Strategy – EXC 2155 – project
732 number 390874280. We thank the DFG for funding the lattice light sheet system through a large
733 equipment grant to KG and JB, project number 413831413. We thank Zeiss for including us in their
734 lattice light-sheet early adaptor program. FJF is holding a graduate student fellowship by the
735 Studienstiftung des deutschen Volkes. The Leibniz Institute for Experimental Virology is supported
736 by the Free and Hanseatic City of Hamburg and the Federal Ministry of Health. KG is further funded
737 by the Free Hanseatic City of Hamburg (grant LFF-FV 71-2019). This study is part of the Leibniz

738 ScienceCampus InterACt (Grant Agreement No. W6/2018). The mass spectrometer used in this
739 study was funded by a Wellcome Trust instrumentation grant 104913/Z/14/Z to KT.

740

741 **Acknowledgments**

742

743 The authors declare no competing interests.

744

745 **References**

746

747

- 748 1. Griffiths P. The direct and indirect consequences of cytomegalovirus infection and potential
749 benefits of vaccination. *Antivir Res.* 2020;176: 104732. doi:10.1016/j.antiviral.2020.104732
- 750 2. Modlin JF, Arvin AM, Fast P, Myers M, Plotkin S, Rabinovich R. Vaccine Development to
751 Prevent Cytomegalovirus Disease: Report from the National Vaccine Advisory Committee. *Clin*
752 *Infect Dis.* 2004;39: 233–239. doi:10.1086/421999
- 753 3. Britt WJ, Prichard MN. New therapies for human cytomegalovirus infections. *Antivir Res.*
754 2018;159: 153–174. doi:10.1016/j.antiviral.2018.09.003
- 755 4. Scrivano L, Sinzger C, Nitschko H, Koszinowski UH, Adler B. HCMV Spread and Cell Tropism
756 are Determined by Distinct Virus Populations. *Plos Pathog.* 2011;7: e1001256.
757 doi:10.1371/journal.ppat.1001256
- 758 5. Adler B. A Viral Pilot for HCMV Navigation? *Viruses.* 2015;7: 3857–3862.
759 doi:10.3390/v7072801
- 760 6. Li G, Nguyen CC, Ryckman BJ, Britt WJ, Kamil JP. A viral regulator of glycoprotein complexes
761 contributes to human cytomegalovirus cell tropism. *Proc National Acad Sci.* 2015;112: 4471–
762 4476. doi:10.1073/pnas.1419875112
- 763 7. Nguyen CC, Siddiquey MNA, Zhang H, Li G, Kamil JP. Human Cytomegalovirus Tropism
764 Modulator UL148 Interacts with SEL1L, a Cellular Factor That Governs Endoplasmic Reticulum-
765 Associated Degradation of the Viral Envelope Glycoprotein gO. *J Virol.* 2018;92: e00688-18.
766 doi:10.1128/jvi.00688-18
- 767 8. Bronzini M, Lugini A, Dell'Oste V, Andrea MD, Landolfo S, Gribaudo G. The US16 Gene of
768 Human Cytomegalovirus Is Required for Efficient Viral Infection of Endothelial and Epithelial
769 Cells. *J Virol.* 2012;86: 6875–6888. doi:10.1128/jvi.06310-11
- 770 9. Lugini A, Cavaletto N, Raimondo S, Geuna S, Gribaudo G. Loss of the Human
771 Cytomegalovirus US16 Protein Abrogates Virus Entry into Endothelial and Epithelial Cells by
772 Reducing the Virion Content of the Pentamer. *J Virol.* 2017;91: e00205-17. doi:10.1128/jvi.00205-
773 17
- 774 10. Owen DJ, Crump CM, Graham SC. Tegument Assembly and Secondary Envelopment of
775 Alphaherpesviruses. *Viruses.* 2015;7: 5084–5114. doi:10.3390/v7092861
- 776 11. Johnson DC, Baines JD. Herpesviruses remodel host membranes for virus egress. *Nat Rev*
777 *Microbiol.* 2011;9: 382–394. doi:10.1038/nrmicro2559
- 778 12. Sanchez V, Greis KD, Sztul E, Britt WJ. Accumulation of Virion Tegument and Envelope
779 Proteins in a Stable Cytoplasmic Compartment during Human Cytomegalovirus Replication:
780 Characterization of a Potential Site of Virus Assembly. *J Virol.* 2000;74: 975–986.
781 doi:10.1128/jvi.74.2.975-986.2000
- 782 13. Procter DJ, Banerjee A, Nukui M, Kruse K, Gaponenko V, Murphy EA, et al. The HCMV
783 Assembly Compartment Is a Dynamic Golgi-Derived MTOC that Controls Nuclear Rotation and
784 Virus Spread. *Dev Cell.* 2018;45: 83-100.e7. doi:10.1016/j.devcel.2018.03.010
- 785 14. Homman-Loudiyi M, Hultenby K, Britt W, Söderberg-Nauclér C. Envelopment of Human
786 Cytomegalovirus Occurs by Budding into Golgi-Derived Vacuole Compartments Positive for gB,
787 Rab 3, Trans-Golgi Network 46, and Mannosidase II. *J Virol.* 2003;77: 3191–3203.
788 doi:10.1128/jvi.77.5.3191-3203.2003

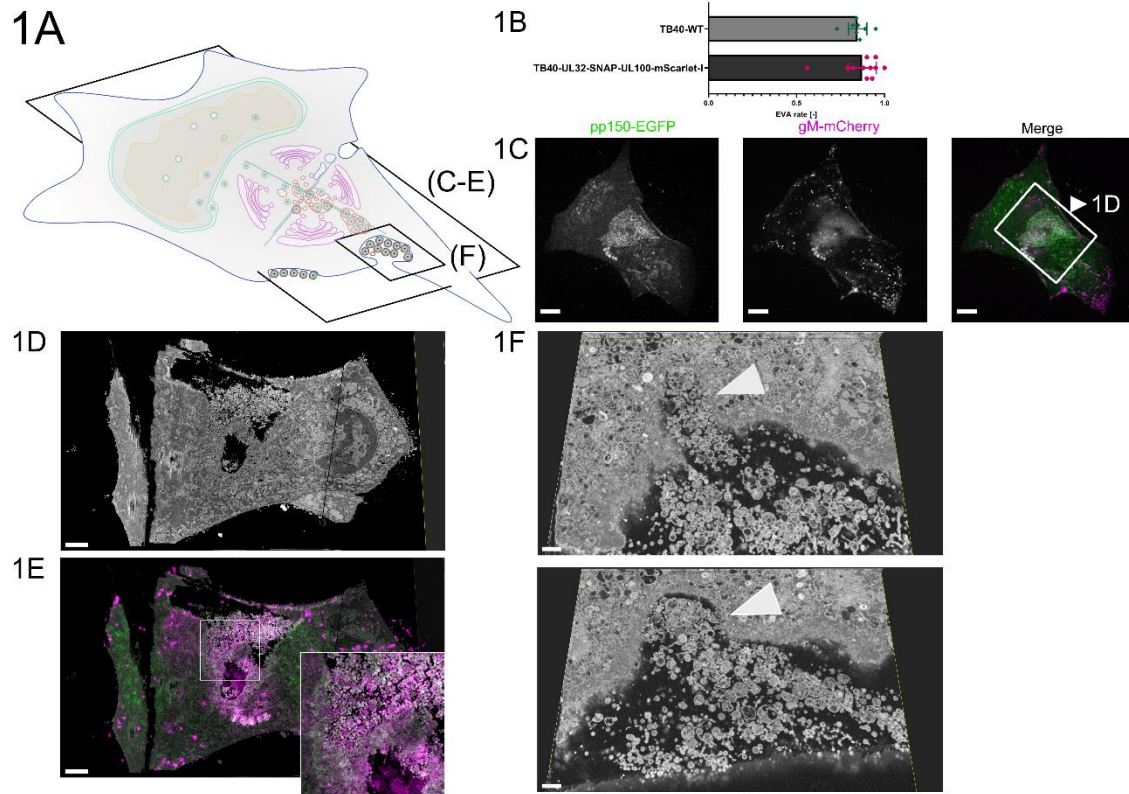
- 789 15. Das S, VasANJI A, Pellett PE. Three-Dimensional Structure of the Human Cytomegalovirus
790 Cytoplasmic Virion Assembly Complex Includes a Reoriented Secretory Apparatus ∇ †. *J Virol.*
791 2007;81: 11861–11869. doi:10.1128/jvi.01077-07
- 792 16. Das S, Pellett PE. Spatial Relationships between Markers for Secretory and Endosomal
793 Machinery in Human Cytomegalovirus-Infected Cells versus Those in Uninfected Cells. *J Virol.*
794 2011;85: 5864–5879. doi:10.1128/jvi.00155-11
- 795 17. Cepeda V, Esteban M, Fraile- Ramos A. Human cytomegalovirus final envelopment on
796 membranes containing both trans- Golgi network and endosomal markers. *Cell Microbiol.*
797 2010;12: 386–404. doi:10.1111/j.1462-5822.2009.01405.x
- 798 18. Moorman NJ, Sharon-Friling R, Shenk T, Cristea IM. A Targeted Spatial-Temporal
799 Proteomics Approach Implicates Multiple Cellular Trafficking Pathways in Human
800 Cytomegalovirus Virion Maturation. *Mol Cell Proteomics.* 2010;9: 851–860.
801 doi:10.1074/mcp.m900485-mcp200
- 802 19. Schauflinger M, Villinger C, Mertens T, Walther P, Einem J. Analysis of human
803 cytomegalovirus secondary envelopment by advanced electron microscopy. *Cell Microbiol.*
804 2013;15: 305–314. doi:10.1111/cmi.12077
- 805 20. Taisne C, Lussignol M, Hernandez E, Moris A, Mouna L, Esclatine A. Human cytomegalovirus
806 hijacks the autophagic machinery and LC3 homologs in order to optimize cytoplasmic
807 envelopment of mature infectious particles. *Sci Rep-uk.* 2019;9: 4560. doi:10.1038/s41598-019-
808 41029-z
- 809 21. Hogue IB, Bosse JB, Hu J-R, Thiberge SY, Enquist LW. Cellular Mechanisms of Alpha
810 Herpesvirus Egress: Live Cell Fluorescence Microscopy of Pseudorabies Virus Exocytosis. *Plos*
811 *Pathog.* 2014;10: e1004535. doi:10.1371/journal.ppat.1004535
- 812 22. Hollinshead M, Johns HL, Sayers CL, Gonzalez- Lopez C, Smith GL, Elliott G. Endocytic
813 tubules regulated by Rab GTPases 5 and 11 are used for envelopment of herpes simplex virus.
814 *Embo J.* 2012;31: 4204–4220. doi:10.1038/emboj.2012.262
- 815 23. Tooze J, Hollinshead M, Reis B, Radsak K, Kern H. Progeny vaccinia and human
816 cytomegalovirus particles utilize early endosomal cisternae for their envelopes. *Eur J Cell Biol.*
817 1993;60: 163–78.
- 818 24. Schauflinger M, Fischer D, Schreiber A, Chevillotte M, Walther P, Mertens T, et al. The
819 Tegument Protein UL71 of Human Cytomegalovirus Is Involved in Late Envelopment and Affects
820 Multivesicular Bodies. *J Virol.* 2011;85: 3821–3832. doi:10.1128/jvi.01540-10
- 821 25. Bughio F, Umashankar M, Wilson J, Goodrum F. Human Cytomegalovirus UL135 and UL136
822 Genes Are Required for Postentry Tropism in Endothelial Cells. *J Virol.* 2015;89: 6536–6550.
823 doi:10.1128/jvi.00284-15
- 824 26. Momtaz S, Molina B, Mlera L, Goodrum F, Wilson JM. Cell type-specific biogenesis of novel
825 vesicles containing viral products in human cytomegalovirus infection. *J Virol.* 2021.
826 doi:10.1128/jvi.02358-20
- 827 27. Butt BG, Owen DJ, Jeffries CM, Ivanova L, Hill CH, Houghton JW, et al. Insights into
828 herpesvirus assembly from the structure of the pUL7:pUL51 complex. *Elife.* 2020;9: e53789.
829 doi:10.7554/elife.53789
- 830 28. Bughio F, Elliott DA, Goodrum F. An Endothelial Cell-Specific Requirement for the UL133-
831 UL138 Locus of Human Cytomegalovirus for Efficient Virus Maturation. *J Virol.* 2013;87: 3062–
832 3075. doi:10.1128/jvi.02510-12
- 833 29. Meissner CS, Suffner S, Schauflinger M, Einem J von, Bogner E. A Leucine Zipper Motif of a
834 Tegument Protein Triggers Final Envelopment of Human Cytomegalovirus. *J Virol.* 2012;86:
835 3370–3382. doi:10.1128/jvi.06556-11
- 836 30. Dietz AN, Villinger C, Becker S, Frick M, Einem J von. A Tyrosine-Based Trafficking Motif of
837 the Tegument Protein pUL71 Is Crucial for Human Cytomegalovirus Secondary Envelopment. *J*
838 *Virol.* 2018;92: e00907-17. doi:10.1128/jvi.00907-17
- 839 31. Mori Y, Koike M, Moriishi E, Kawabata A, Tang H, Oyaizu H, et al. Human Herpesvirus- 6
840 Induces MVB Formation, and Virus Egress Occurs by an Exosomal Release Pathway. *Traffic.*
841 2008;9: 1728–1742. doi:10.1111/j.1600-0854.2008.00796.x

- 842 32. Sampaio K, Jahn G, Sinzger C. Virus-Host Interactions, Methods and Protocols. *Methods Mol*
843 *Biology* Clifton N J. 2013;1064: 201–209. doi:10.1007/978-1-62703-601-6_14
- 844 33. Mingo RM, Han J, Newcomb WW, Brown JC. Replication of Herpes Simplex Virus: Egress of
845 Progeny Virus at Specialized Cell Membrane Sites. *J Virol.* 2012;86: 7084–7097.
846 doi:10.1128/jvi.00463-12
- 847 34. Bebelman MP, Bun P, Huvneers S, Niel G van, Pegtel DM, Verweij FJ. Real-time imaging of
848 multivesicular body–plasma membrane fusion to quantify exosome release from single cells. *Nat*
849 *Protoc.* 2020;15: 102–121. doi:10.1038/s41596-019-0245-4
- 850 35. Dang VD, Jella KK, Ragheb RRT, Denslow ND, Alli AA. Lipidomic and proteomic analysis of
851 exosomes from mouse cortical collecting duct cells. *Faseb J.* 2017;31: 5399–5408.
852 doi:10.1096/fj.201700417r
- 853 36. Turner DL, Korneev DV, Purdy JG, Marco A de, Mathias RA. The host exosome pathway
854 underpins biogenesis of the human cytomegalovirus virion. *Elife.* 2020;9: e58288.
855 doi:10.7554/elife.58288
- 856 37. Streck NT, Zhao Y, Sundstrom JM, Buchkovich NJ. Human Cytomegalovirus Utilizes
857 Extracellular Vesicles to Enhance Virus Spread. *J Virol.* 2020. doi:10.1128/jvi.00609-20
- 858 38. Hashimoto Y, Sheng X, Murray-Nerger LA, Cristea IM. Temporal dynamics of protein complex
859 formation and dissociation during human cytomegalovirus infection. *Nat Commun.* 2020;11: 806.
860 doi:10.1038/s41467-020-14586-5
- 861 39. Varnum SM, Streblov DN, Monroe ME, Smith P, Auberry KJ, Paša-Tolić L, et al. Identification
862 of Proteins in Human Cytomegalovirus (HCMV) Particles: the HCMV Proteome. *J Virol.* 2004;78:
863 10960–10966. doi:10.1128/jvi.78.20.10960-10966.2004
- 864 40. Piper RC, Luzio JP. Late Endosomes: Sorting and Partitioning in Multivesicular Bodies.
865 *Traffic.* 2001;2: 612–621. doi:10.1034/j.1600-0854.2001.20904.x
- 866 41. Jiang B, Himmelsbach K, Ren H, Boller K, Hildt E. Subviral Hepatitis B Virus Filaments, like
867 Infectious Viral Particles, Are Released via Multivesicular Bodies. *J Virol.* 2016;90: 3330–3341.
868 doi:10.1128/jvi.03109-15
- 869 42. Datta A, Kim H, McGee L, Johnson AE, Talwar S, Marugan J, et al. High-throughput
870 screening identified selective inhibitors of exosome biogenesis and secretion: A drug repurposing
871 strategy for advanced cancer. *Sci Rep-uk.* 2018;8: 8161. doi:10.1038/s41598-018-26411-7
- 872 43. Khan FM, Saleh E, Alawadhi H, Harati R, Zimmermann W-H, El-Awady R. Inhibition of
873 exosome release by Ketotifen enhances sensitivity of cancer cells to doxorubicin. *Cancer Biol*
874 *Ther.* 2017;19: 1–9. doi:10.1080/15384047.2017.1394544
- 875 44. Zhang H, Lu J, Liu J, Zhang G, Lu A. Advances in the discovery of exosome inhibitors in
876 cancer. *J Enzym Inhib Med Ch.* 2020;35: 1322–1330. doi:10.1080/14756366.2020.1754814
- 877 45. Hogue IB, Scherer J, Enquist LW. Exocytosis of Alphaherpesvirus Virions, Light Particles, and
878 Glycoproteins Uses Constitutive Secretory Mechanisms. *Mbio.* 2016;7: e00820-16.
879 doi:10.1128/mbio.00820-16
- 880 46. Maninger S, Bosse JB, Lemnitzer F, Pogoda M, Mohr CA, Einem J von, et al. M94 Is
881 Essential for the Secondary Envelopment of Murine Cytomegalovirus †. *J Virol.* 2011;85: 9254–
882 9267. doi:10.1128/jvi.00443-11
- 883 47. Hogue IB. Tegument Assembly, Secondary Envelopment and Exocytosis. *Curr Issues Mol*
884 *Biol.* 2022;42: 551–604. doi:10.21775/cimb.042.551
- 885 48. Théry C, Zitvogel L, Amigorena S. Exosomes: composition, biogenesis and function. *Nat Rev*
886 *Immunol.* 2002;2: 569–579. doi:10.1038/nri855
- 887 49. Cocucci E, Racchetti G, Meldolesi J. Shedding microvesicles: artefacts no more. *Trends Cell*
888 *Biol.* 2009;19: 43–51. doi:10.1016/j.tcb.2008.11.003
- 889 50. Colombo M, Raposo G, Théry C. Biogenesis, Secretion, and Intercellular Interactions of
890 Exosomes and Other Extracellular Vesicles. *Annu Rev Cell Dev Bi.* 2014;30: 1–35.
891 doi:10.1146/annurev-cellbio-101512-122326
- 892 51. Crump CM, Yates C, Minson T. Herpes Simplex Virus Type 1 Cytoplasmic Envelopment
893 Requires Functional Vps4 †. *J Virol.* 2007;81: 7380–7387. doi:10.1128/jvi.00222-07

- 894 52. Pawliczek T, Crump CM. Herpes Simplex Virus Type 1 Production Requires a Functional
895 ESCRT-III Complex but Is Independent of TSG101 and ALIX Expression ∇ . *J Virol.* 2009;83:
896 11254–11264. doi:10.1128/jvi.00574-09
- 897 53. Kharkwal H, Smith CG, Wilson DW. Blocking ESCRT-Mediated Envelopment Inhibits
898 Microtubule-Dependent Trafficking of Alphaherpesviruses In Vitro. *J Virol.* 2014;88: 14467–
899 14478. doi:10.1128/jvi.02777-14
- 900 54. Tandon R, AuCoin DP, Mocarski ES. Human Cytomegalovirus Exploits ESCRT Machinery in
901 the Process of Virion Maturation ∇ . *J Virol.* 2009;83: 10797–10807. doi:10.1128/jvi.01093-09
- 902 55. Fraile- Ramos A, Pelchen- Matthews A, Risco C, Rejas MT, Emery VC, Hassan- Walker AF,
903 et al. The ESCRT machinery is not required for human cytomegalovirus envelopment. *Cell*
904 *Microbiol.* 2007;9: 2955–2967. doi:10.1111/j.1462-5822.2007.01024.x
- 905 56. Streck NT, Carmichael J, Buchkovich NJ. Nonenvelopment Role for the ESCRT-III Complex
906 during Human Cytomegalovirus Infection. *J Virol.* 2018;92: e02096-17. doi:10.1128/jvi.02096-17
- 907 57. Yáñez-Mó M, Barreiro O, Gordon-Alonso M, Sala-Valdés M, Sánchez-Madrid F. Tetraspanin-
908 enriched microdomains: a functional unit in cell plasma membranes. *Trends Cell Biol.* 2009;19:
909 434–446. doi:10.1016/j.tcb.2009.06.004
- 910 58. Takino T, Miyamori H, Kawaguchi N, Uekita T, Seiki M, Sato H. Tetraspanin CD63 promotes
911 targeting and lysosomal proteolysis of membrane-type 1 matrix metalloproteinase. *Biochem*
912 *Bioph Res Co.* 2003;304: 160–166. doi:10.1016/s0006-291x(03)00544-8
- 913 59. van Niel G, Charrin S, Simoes S, Romao M, Rochin L, Saftig P, et al. The Tetraspanin CD63
914 Regulates ESCRT-Independent and -Dependent Endosomal Sorting during Melanogenesis. *Dev*
915 *Cell.* 2011;21: 708–721. doi:10.1016/j.devcel.2011.08.019
- 916 60. Perez-Hernandez D, Gutiérrez-Vázquez C, Jorge I, López-Martín S, Ursa A, Sánchez-Madrid
917 F, et al. The Intracellular Interactome of Tetraspanin-enriched Microdomains Reveals Their
918 Function as Sorting Machineries toward Exosomes. *J Biol Chem.* 2013;288: 11649–11661.
919 doi:10.1074/jbc.m112.445304
- 920 61. Zicari S, Arakelyan A, Palomino RAÑ, Fitzgerald W, Vanpouille C, Lebedeva A, et al. Human
921 cytomegalovirus-infected cells release extracellular vesicles that carry viral surface proteins.
922 *Virology.* 2018;524: 97–105. doi:10.1016/j.virol.2018.08.008
- 923 62. Kosaka N, Iguchi H, Yoshioka Y, Takeshita F, Matsuki Y, Ochiya T. Secretory Mechanisms
924 and Intercellular Transfer of MicroRNAs in Living Cells. *J Biol Chem.* 2010;285: 17442–17452.
925 doi:10.1074/jbc.m110.107821
- 926 63. Murrell I, Tomasec P, Wilkie GS, Dargan DJ, Davison AJ, Stanton RJ. Impact of Sequence
927 Variation in the UL128 Locus on Production of Human Cytomegalovirus in Fibroblast and
928 Epithelial Cells. *J Virol.* 2013;87: 10489–10500. doi:10.1128/jvi.01546-13
- 929 64. Murrell I, Bedford C, Ladell K, Miners KL, Price DA, Tomasec P, et al. The pentameric
930 complex drives immunologically covert cell–cell transmission of wild-type human
931 cytomegalovirus. *Proc National Acad Sci.* 2017;114: 6104–6109. doi:10.1073/pnas.1704809114
- 932 65. Radsak K, Eickmann M, Mockenhaupt T, Bogner E, Kern H, Eis-Hübinger A, et al. Retrieval
933 of human cytomegalovirus glycoprotein B from the infected cell surface for virus envelopment.
934 *Arch Virol.* 1996;141: 557–572. doi:10.1007/bf01718317
- 935 66. Tugizov S, Maidji E, Xiao J, Pereira L. An Acidic Cluster in the Cytosolic Domain of Human
936 Cytomegalovirus Glycoprotein B Is a Signal for Endocytosis from the Plasma Membrane. *J Virol.*
937 1999;73: 8677–8688. doi:10.1128/jvi.73.10.8677-8688.1999
- 938 67. Calistri A, Sette P, Salata C, Cancellotti E, Forghieri C, Comin A, et al. Intracellular Trafficking
939 and Maturation of Herpes Simplex Virus Type 1 gB and Virus Egress Require Functional
940 Biogenesis of Multivesicular Bodies ∇ . *J Virol.* 2007;81: 11468–11478. doi:10.1128/jvi.01364-07
- 941 68. Dogramatzis C, Deschamps T, Kalamvoki M. Biogenesis of extracellular vesicles during
942 herpes simplex virus type 1 infection: The role of the CD63 tetraspanin. *J Virol.* 2018;93:
943 JVI.01850-18. doi:10.1128/jvi.01850-18
- 944 69. Filippakis H, Spandidos DA, Sourvinos G. Herpesviruses: Hijacking the Ras signaling
945 pathway. *Biochimica Et Biophysica Acta Bba - Mol Cell Res.* 2010;1803: 777–785.
946 doi:10.1016/j.bbamcr.2010.03.007

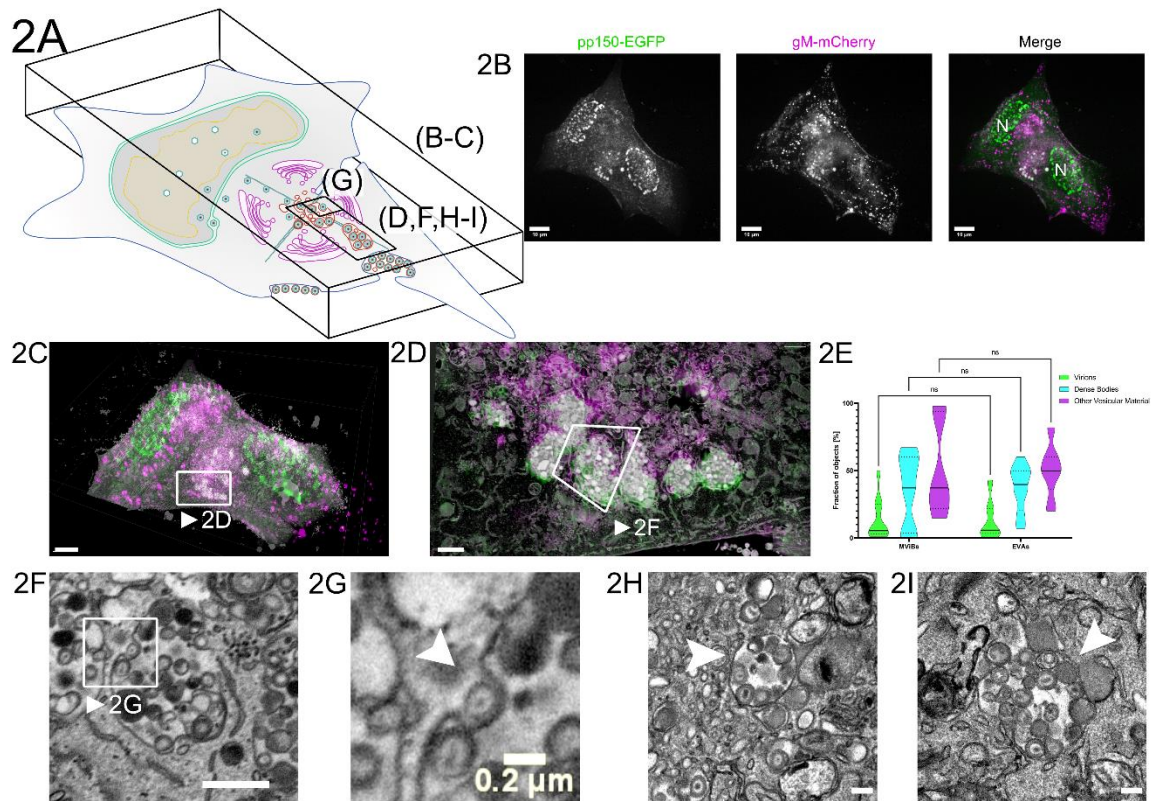
- 947 70. Filippakis H, Dimitropoulou P, Eliopoulos AG, Spandidos DA, Sourvinos G. The enhanced
948 host-cell permissiveness of human cytomegalovirus is mediated by the Ras signaling pathway.
949 *Biochimica Et Biophysica Acta Bba - Mol Cell Res.* 2011;1813: 1872–1882.
950 doi:10.1016/j.bbamcr.2011.07.003
- 951 71. Farassati F, Yang A-D, Lee Pwk. Oncogenes in Ras signalling pathway dictate host-cell
952 permissiveness to herpes simplex virus 1. *Nat Cell Biol.* 2001;3: 745–750. doi:10.1038/35087061
- 953 72. Sinzger C, Hahn G, Digel M, Katona R, Sampaio KL, Messerle M, et al. Cloning and
954 sequencing of a highly productive, endotheliotropic virus strain derived from human
955 cytomegalovirus TB40/E. *J Gen Virol.* 2008;89: 359–368. doi:10.1099/vir.0.83286-0
- 956 73. Walton J. Lead aspartate, an en bloc contrast stain particularly useful for ultrastructural
957 enzymology. *J Histochem Cytochem Official J Histochem Soc.* 1979;27: 1337–1342.
958 doi:10.1177/27.10.512319
- 959 74. Tischer BK, Smith GA, Osterrieder N. In *Vitro Mutagenesis Protocols*, Third Edition. 2010;
960 421–430. doi:10.1007/978-1-60761-652-8_30
- 961 75. Bindels DS, Haarbosch L, Weeren L van, Postma M, Wiese KE, Mastop M, et al. mScarlet: a
962 bright monomeric red fluorescent protein for cellular imaging. *Nat Methods.* 2016;14: nmeth.4074.
963 doi:10.1038/nmeth.4074
- 964 76. Talbot P, Almeida JD. Human Cytomegalovirus: Purification of Enveloped Virions and Dense
965 Bodies. *J Gen Virol.* 1977;36: 345–349. doi:10.1099/0022-1317-36-2-345
- 966 77. Distler U, Kuharev J, Navarro P, Tenzer S. Label-free quantification in ion mobility–enhanced
967 data-independent acquisition proteomics. *Nat Protoc.* 2016;11: 795–812.
968 doi:10.1038/nprot.2016.042
- 969 78. Silva JC, Gorenstein MV, Li G-Z, Vissers JPC, Geromanos SJ. Absolute Quantification of
970 Proteins by LCMSE A Virtue of Parallel ms Acquisition. *Mol Cell Proteomics.* 2006;5: 144–156.
971 doi:10.1074/mcp.m500230-mcp200
- 972 79. Zhu H, Shen Y, Shenk T. Human cytomegalovirus IE1 and IE2 proteins block apoptosis. *J*
973 *Virol.* 1995;69: 7960–7970. doi:10.1128/jvi.69.12.7960-7970.1995
- 974
975
976

977 **Figures and Tables**



978
979

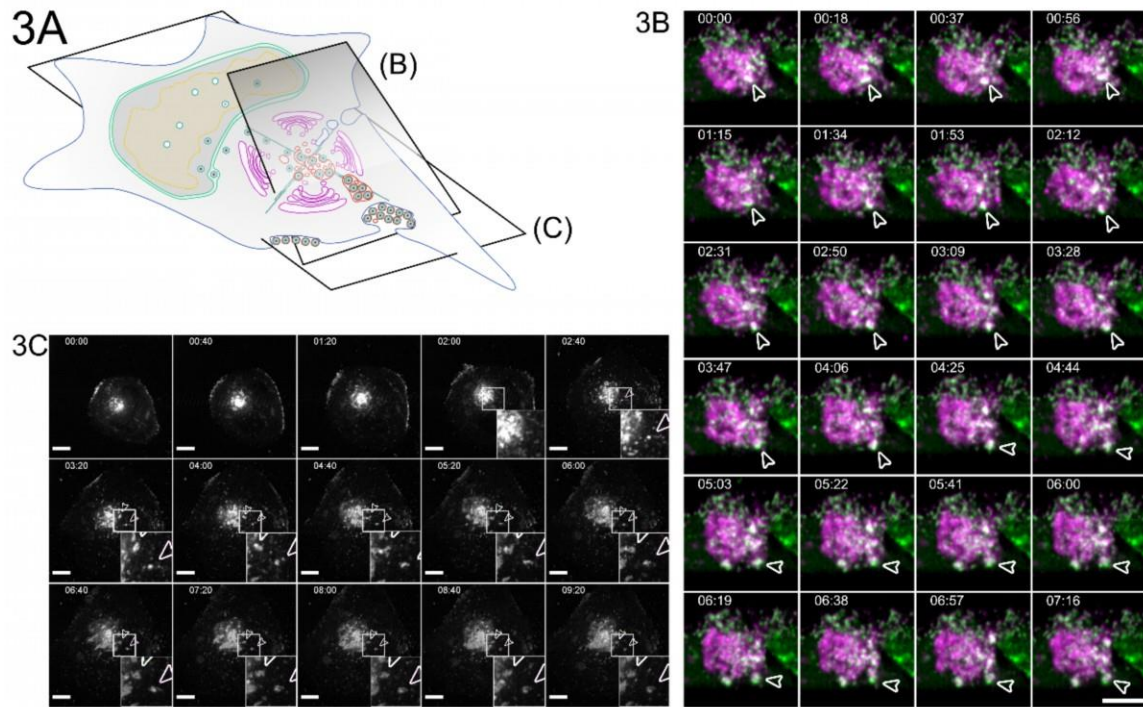
980 **Figure 1. EVAs are extracellular accumulations of viral products and other vesicular**
981 **material. 1A** Overview indicates the subfigures' positions in relation to the whole cell. **1B**
982 **Quantification of EVA occurrence.** HFF cells were infected with HCMV-pp150-SNAP-gM-mScarlet-
983 **I** or HCMV-TB40-WT at an MOI of 1 and fixed at 120 hpi. HCMV-TB40-WT infected cells were
984 **stained for gB.** Late-infected cells were counted, and the rate of EVAs was quantified. Borders
985 **show the 95% confidence interval of the mean.** N=269 from 11 replicates for HCMV-pp150-SNAP-
986 **gM-mScarlet-I** and N=750 from 8 replicates for HCMV-TB40-WT. No significant difference could
987 **be found.** **1C** Spinning-disk confocal section of HFF-wt cells infected with HCMV-pp150-EGFP-gM-
988 **mCherry (MOI = 3)** at 4 dpi, showing EVAs positive for pp150-EGFP (green) and gM-mCherry
989 **(magenta)** close to the plasma membrane. Scale bar represents 10 μm . **1D/E** CLEM of the area
990 **marked in 1C.** **1D** Rendering of SBF-SEM data depicting the area close and below the plasma
991 **membrane.** Scale bar represents 3 μm . **1E** Correlative overlay of SBF-SEM data from 1D with the
992 **corresponding fluorescence data from 1C** indicating that pp150-SNAP and gM-mScarlet-I positive
993 **EVAs are located outside the cell.** Scale bar represents 3 μm . **1F** Two z-slices are depicting
994 **invaginations (white arrowheads)** next to an EVA that can be found in SBF-SEM data along the cell
995 **surface.** Scale bars represent 700 nm.



996
997

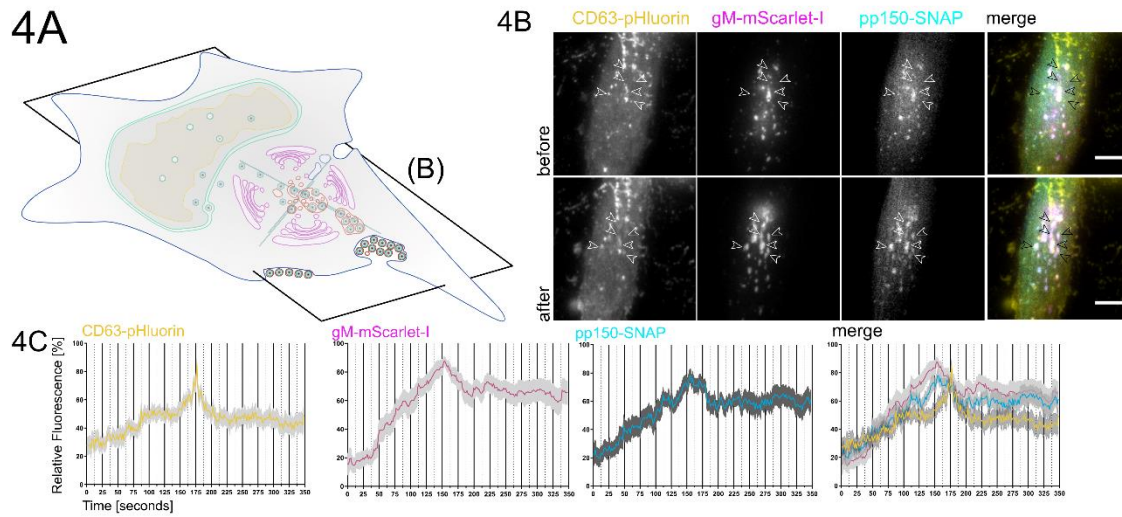
998 **Figure 2 Correlative fluorescence and EM detect MVIBs filled with virus progeny.** **2A** Overview
 999 indicates the subfigures' positions in relation to the whole cell. CLEM of HFF-cells infected with
 1000 HCMV-pp150-EGFP-gM-mCherry (MOI = 3) at 4 dpi. **2B** Maximum z-projection of a 3D spinning-
 1001 disk confocal microscopy stack. pp150-EGFP is colored in green and gM-mCherry signals in
 1002 magenta. N marks nuclei. Scale bar indicates 10 μm . **2C** Correlative overlay of the fluorescence
 1003 data shown in 2B and corresponding SBF-SEM data. Scale bar indicates 7 μm . The white frame
 1004 marks MVIBs. See also Sup. Vid. 3B. **2D** Correlative rendering of MVIBs highlighted in 2C. The
 1005 white frame marks one MVIB detailed in 2F **2E** Quantitative comparison of MVIB and EVA contents.
 1006 Statistical analysis was performed with a 2-way ANOVA and Šídák's multiple comparisons test. No
 1007 significant differences in the contents of MVIBs and EVAs could be found. **2F** Section from the
 1008 rendered SBF-SEM stack shown in 2D. Image signals were inverted to facilitate comparison with
 1009 TEM images. An HCMV capsid budding into an MVIB is highlighted (white arrow). Also, refer to
 1010 Sup. Vid. 3A-B for a 3D rendering of the presented data. Scale bar indicates 1 μm . **2G** Insert from
 1011 2G. Arrow marks inwards budding viral capsid. Scale bar indicates 0.2 μm . **2H-I** HFF cells were
 1012 infected with HCMV-TB40-WT at an MOI of 5, fixed, and processed for EM as described for SBF-
 1013 SEM at 120 hpi with the modification that the cells were embedded for classical sectioning in Epon
 1014 without conductive fillers. Filled arrowheads indicate MVIBs filled with virus progeny. All scale bars
 1015 represent 0.2 μm .

1016



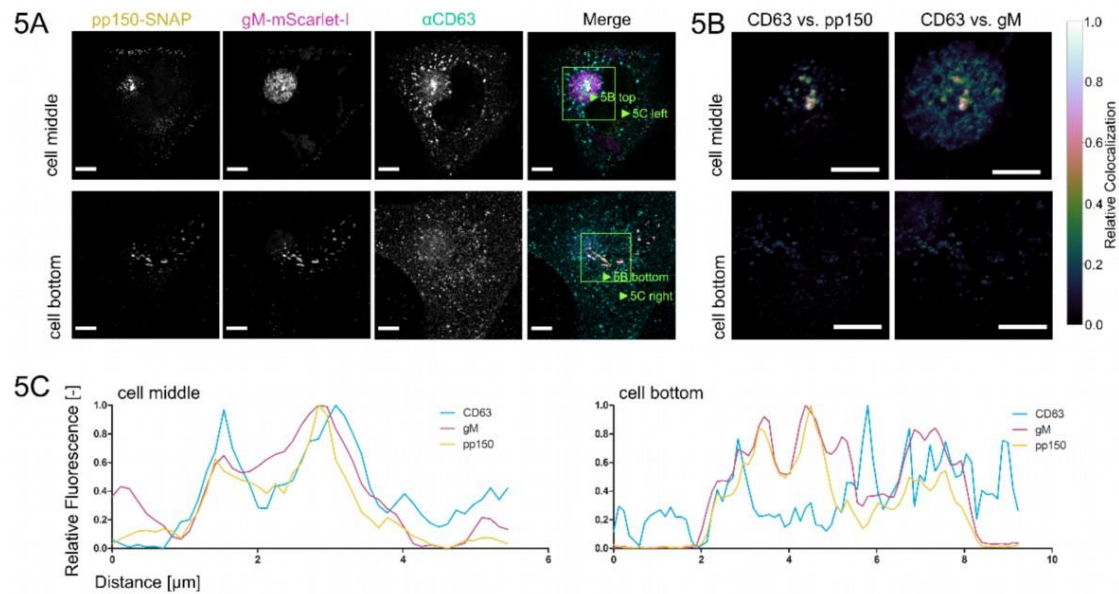
1017
1018
1019
1020
1021
1022
1023
1024
1025
1026
1027
1028
1029
1030

Figure 3. Bulk release from MViBs leads to EVA formation. **3A** Overview indicates the subfigures' positions in relation to the whole cell. **3B** HFF cells were infected with HCMV-pp150-EGFP-gM-mCherry at an MOI of 1. At 96 hpi, the cells were imaged by lattice light-sheet microscopy, taking whole-cell volumes every 2.11 seconds at a 30° angle to the growth substrate. Maximum projections of 20 slices with a total depth of 2 μm of an area under the viral AC and incorporating the plasma membrane are shown. White arrowheads highlight an MViB positive for pp150-EGFP (green) and gM-mCherry (magenta) that approaches the plasma membrane and relaxes at it. Also, refer to Sup. Vid. 5 for a rendering and several side views. **3C** HFF cells were infected with HCMV-pp150-SNAP-gM-mScarlet-I at an MOI of 1. At 72 hpi, cells were imaged live with confocal spinning-disk microscopy. Only the gM-mScarlet-I channel is shown. Both channels can be seen in Sup. Vid. 7. The formation of two EVAs is highlighted with white arrowheads. Scale bar indicates 10 μm. The time format is hh:mm. Also, refer to Sup. Vid. 6 and 7.



1031
1032
1033
1034
1035
1036
1037
1038
1039
1040
1041
1042
1043

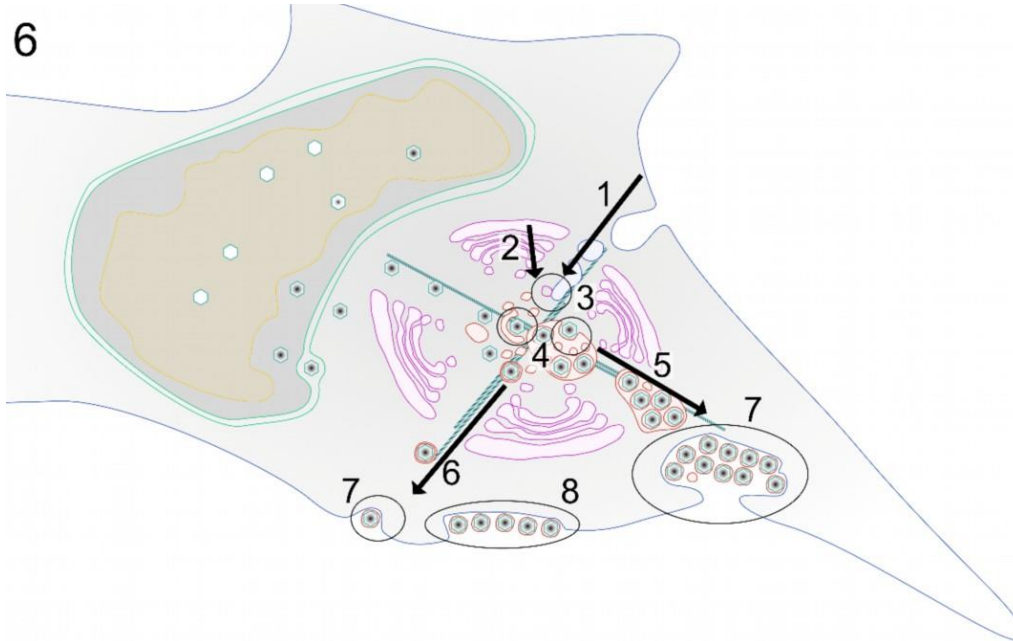
Figure 4. EVAs are the result of fusion events between MViBs and the plasma membrane.
4A Overview indicates the subfigures' positions in relation to the whole cell. HFF-CD63-pHluorin were infected with HCMV-pp150-SNAP-gM-mScarlet-I at an MOI of 0.6 and imaged at 72 and 96 hpi by fluorescence microscopy under TIRF conditions for 1h at an average frame rate of 0.57 frames per second (fps). **4B** TIRF images of a cell before (upper row labeled with before) and after (lower row of images labeled "after") bulk release events from MViBs occurred. Positions of EVA formation are marked by the white arrows (black in the merge). Scale bar indicates 10 μ m. **4C** Quantification of fluorescence signals during EVA formation events over time. Solid lines are averages from 14 EVA formation events extracted from 5 different cells chosen from 4 replicates of infections. Grey areas show the standard error of the mean.



1044
1045
1046
1047
1048
1049
1050
1051
1052
1053
1054
1055
1056
1057
1058

Figure 5. Tetraspanin CD63 localizes to MVIBs. 5A HFF cells were infected at an MOI of 1 with HCMV-pp150-SNAP-gM-mScarlet-I, fixed at 4 dpi, stained for CD63, and whole cells were imaged using confocal laser scanning microscopy. From a representative cell, two slices are shown. One slice depicts the middle of the cell (cell middle), and one depicts the plasma membrane level (cell bottom). The fluorescence pattern of CD63 (α CD63) was compared to gM (gM-mScarlet-I), and pp150 (pp150-SNAP). In the cell's center, CD63 localized to the assembly complex' center and marked MVIBs in the cytoplasm, which were pp150 and gM positive. At the plasma membrane, EVAs were positive for pp150 and gM signals but lacked CD63. 5B Spatially weighted colocalization analysis shows areas in the assembly complex where CD63 colocalization with MVIBs is especially pronounced (cell middle). No significant colocalization between CD63 and pp150 or gM is present in EVAs (cell bottom). All scale bars (5A and 5B) indicate 10 μ m. 5C Line plots for the indicated areas in 5B.

1059



1060

1061

1062

1063

1064

1065

1066

1067

1068

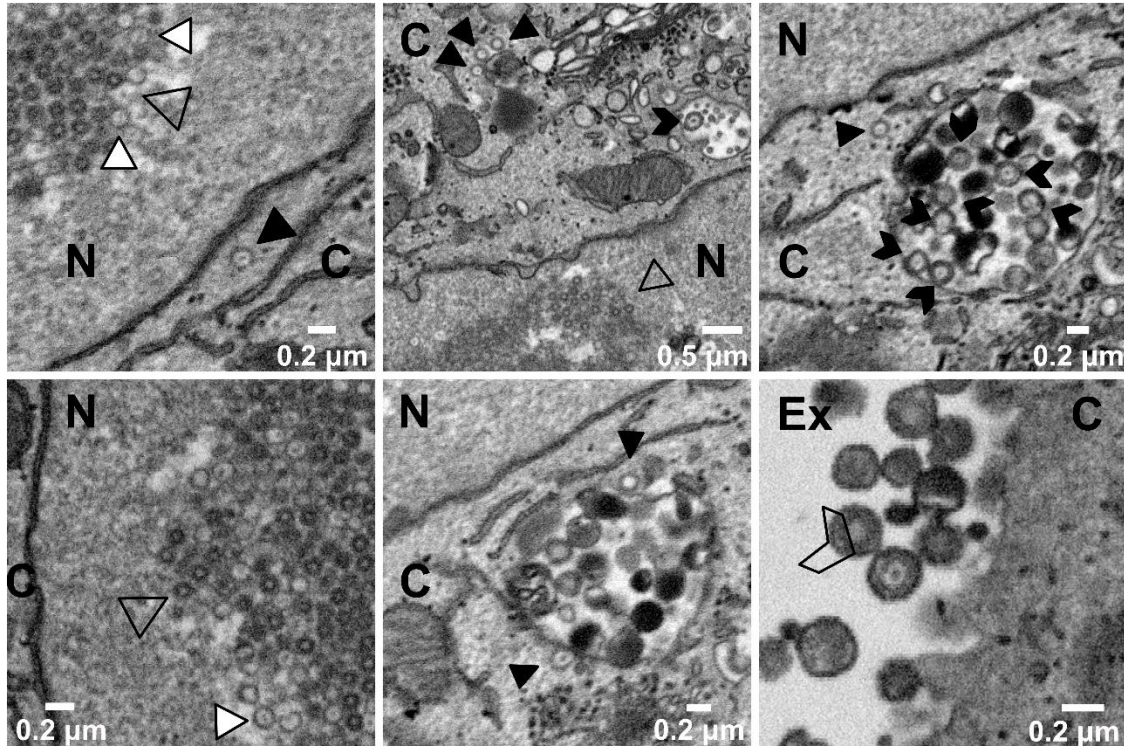
Figure 6. Model of possible HCMV release pathways. 1-3 Membranes of late-endosomal and trans-Golgi origin are trafficked to the center of the assembly complex and subsequently utilized for secondary envelopment. 4 After egress from the nucleus, capsids are trafficked to the assembly complex where they either bud individually into single vesicles or into MViBs to acquire their membrane envelope. 5-6 Virus-containing vesicles and MVBs are transported towards the plasma membrane, and 7 fuse with it to release their content to the extracellular space. 8 MViB fusion leads to EVA formation.

1069 **Table 1. Sequences for 2-Step BAC mutagenesis of HCMV-TB40-pp150-SNAP-gM-**
 1070 **mScarlet-I.**
 1071

TB40-pp150-SNAP Insert Sequence	
Insert Sequence	<p>CACACGGAGGATCCACCGGTCGCCACC atggacaagactgcgaaatgaagcgcaccaccctg gatagccctctgggcaagctggaactgtctgggtgcg aacagggcctgcacgagatcaagctgctgggcaaag gaacatctgccgccgacgccgtggaagtgcctgccc agccgccgtgctgggaggaccagagccactgatgca ggccaccgcctggctcaacgcctactttcaccagcctg aggccatcgaggagtccctgtgccagccctgcaccac ccagtgtccagcaggagagctttaccgccaggtgct gtggaaactgctgaaagtgggaagttcggagaggta tcagctaccagcagctggccgccctggccggcaatcc cgccgccaccgccgccgtgaaaccgccctgagcgg aatcccgtgccattctgatcccctgccaccgggtggt gtctagctctggcgccgtggggggctacgagggcggg ctgccgtgaaagagtggctgctggcccacgagggcc acagactgggcaagcctgggctgggt</p>
TB40-gM-mScarlet-I Primer (50bp overhangs)	
Forward	<p>ACT ATC ACG TCG TGG ACT TTG AAA GGC TCA ACA TGT CGG CCT ACA ACG TAG TGA GCA AGG GCG AGG C</p>
Reverse	<p>CAC ACC AGC TGC ACC GAG TCT AAG AAA AGC ATA GGC GTG TGC AGG TGC ATC TTG TAC AGC TCG TCC ATG CC</p>

1072
 1073
 1074

Supplementary Figure 1

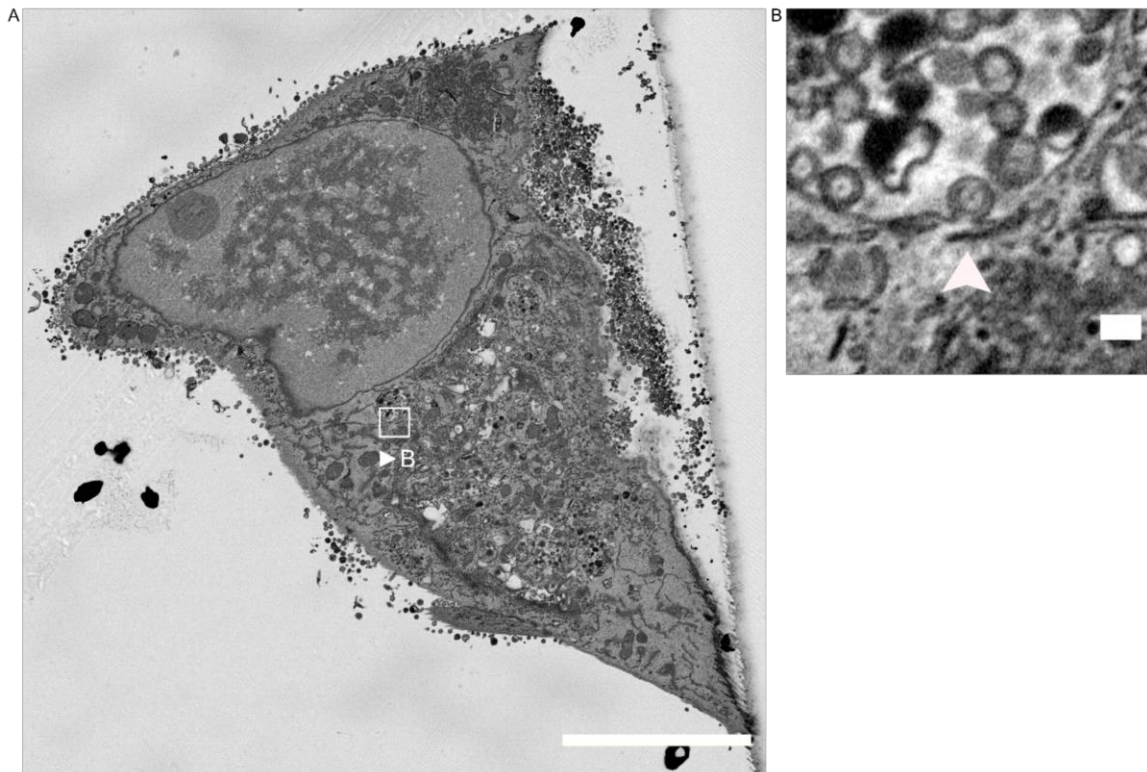


1075

1076 **Supplementary Figure 1. SBF-SEM can visualize all steps of HCMV virus particle**
1077 **morphogenesis.** HFF cells were infected with HCMV-pp150-EGFP-gM-mCherry (MOI 3) and
1078 processed for EM 4 dpi. Image signals were inverted to facilitate comparison with TEM images. N
1079 marks nucleoplasm, C indicates cytoplasm, and Ex the extracellular space. Highlighted in the
1080 panels are examples of B-capsids in the nucleus (unfilled black triangles), DNA- filled nuclear C-
1081 capsids (white triangles with black contour), cytoplasmic non-enveloped C-capsids (black
1082 triangles), intracellular, enveloped virus particles (black filled arrowheads) as well as enveloped,
1083 released particles (empty arrowhead with black contour). Scale bar lengths are specified in each
1084 image.

1085

Supplementary Figure 2

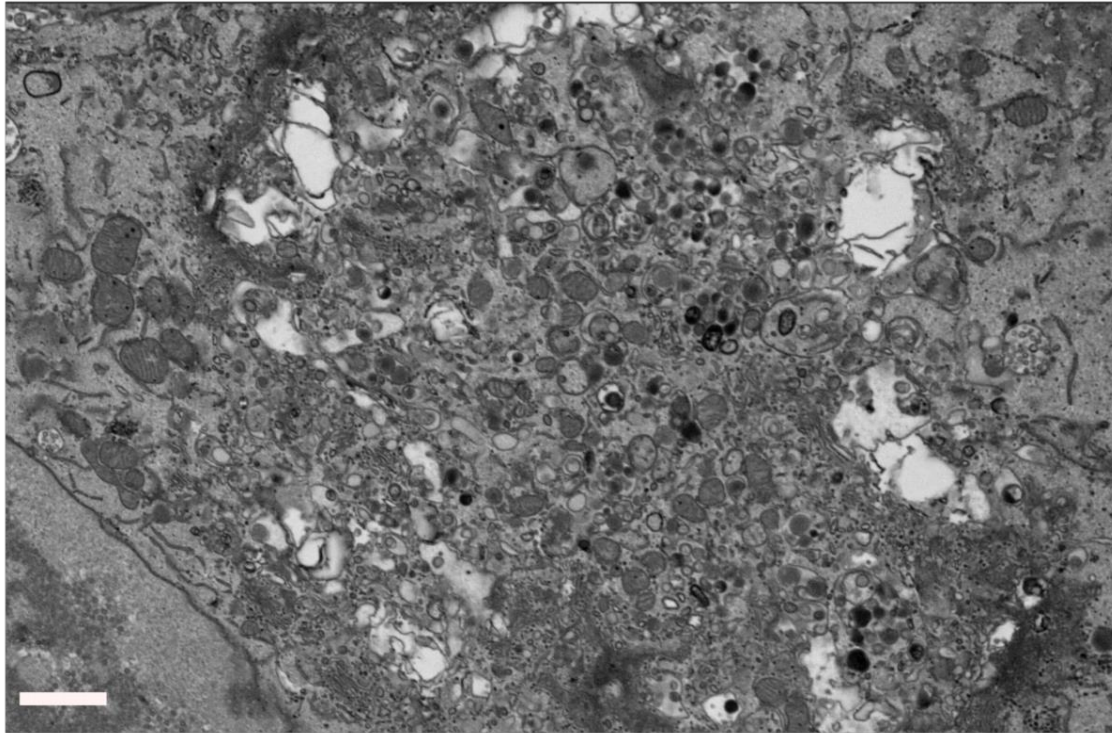


1086

1087 **Supplementary Figure 2. Particle budding at MViBs in relation to the infected cell**
1088 **architecture. S2A** Single SBF-SEM section of an infected HFF cell. HFF cell infected with HCMV-
1089 pp150-EGFP-gM-mCherry (MOI 3) at 4dpi. Image signals were inverted to facilitate comparison
1090 with TEM images. The white frame indicates the area cropped and enlarged in B, showing the
1091 surface of an MViB in the periphery of the assembly complex. Scale bar indicates 10 μ m. **S2B** A
1092 detail showing a single particle budding into an MViB (white arrowhead). Scale bar indicates
1093 200nm.

1094

Supplementary Figure 3

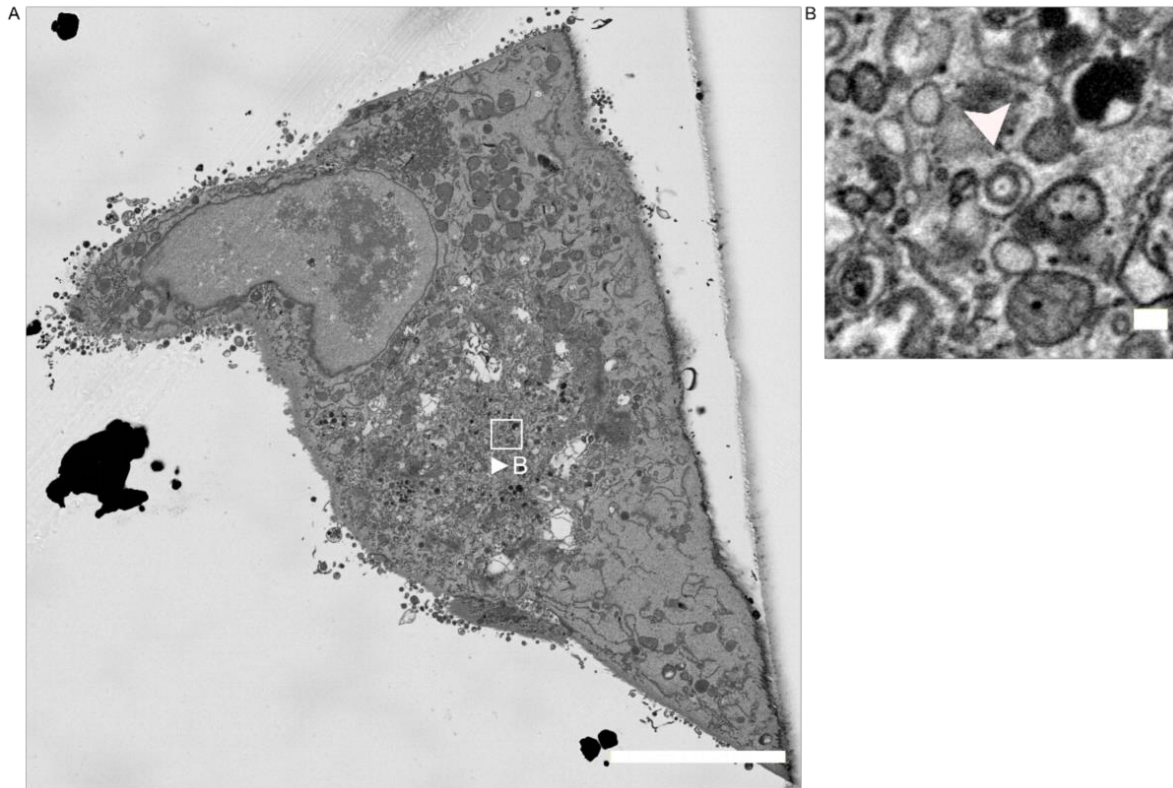


1095

1096 **Supplementary Figure 3. Overview of an HCMV assembly complex in an infected HFF cell.**
1097 HFF cell infected with HCMV-pp150-EGFP-gM-mCherry (MOI 3) at 4dpi. Shown is the assembly
1098 complex in a resliced section through an SBF-SEM stack. Scale bar indicates 1.5 μ m. Image
1099 signals were inverted to facilitate comparison with TEM images.

1100

Supplementary Figure 4

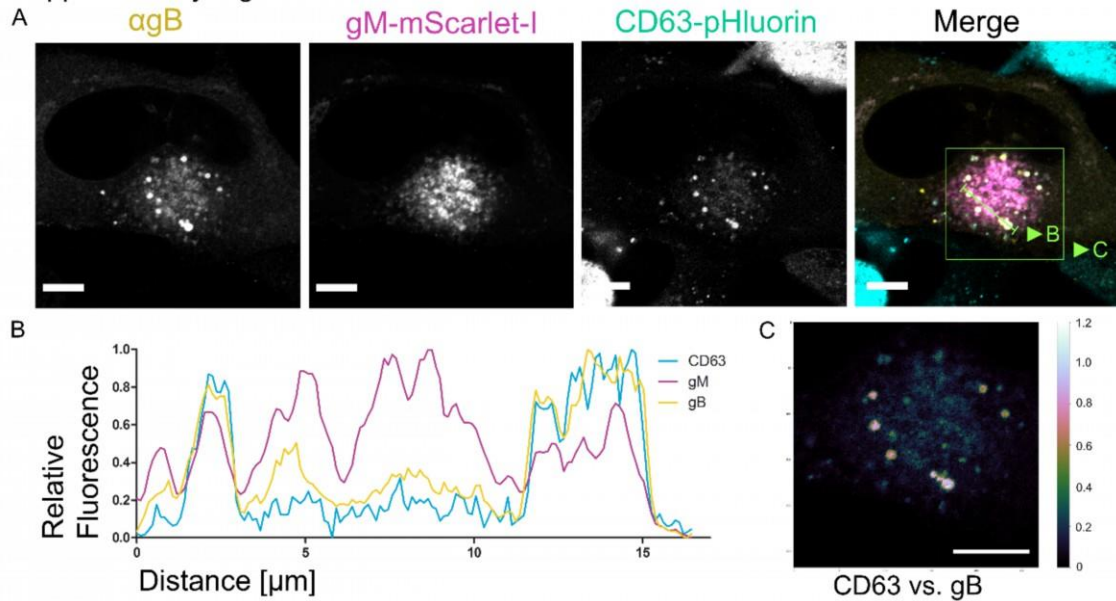


1101

1102 **Supplementary Figure 4. Virus particle budding into an individual small vesicle. S4A** Single
1103 SBF-SEM section of an infected HFF cell. HFF cell infected with HCMV-pp150-EGFP-gM-mCherry
1104 (MOI 3) at 4dpi. The white frame indicates the area cropped and enlarged in B. Scale bar indicates
1105 10 μm . **S4B** A detail showing a single capsid budding into a single vesicle (white arrowhead). Scale
1106 bar indicates 200 nm. Image signals were inverted to facilitate comparison with TEM images.

1107

Supplementary Figure 5

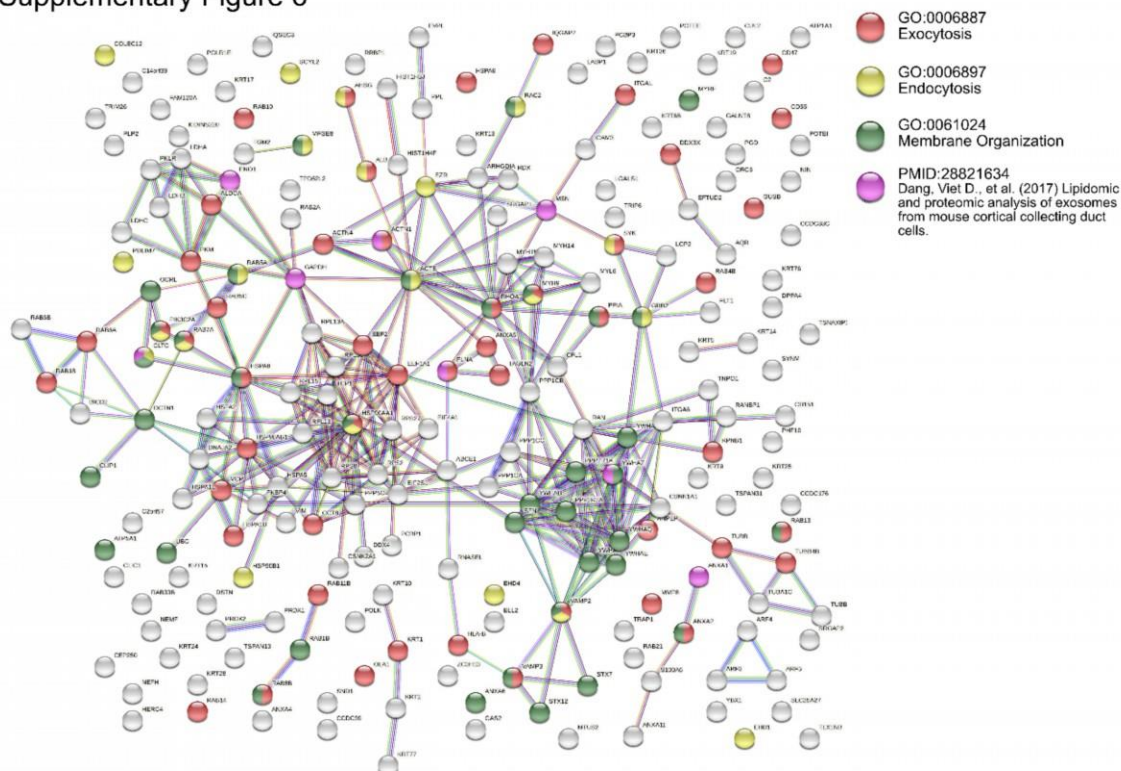


1108

1109 **Supplementary Figure 5. Tetraspanin CD63 colocalizes with gM and gB.** S5A HFF-CD63-
1110 pHluorin cells were infected at an MOI of 1 with HCMV-pp150-SNAP-gM-mScarlet-I. Cells were
1111 fixed at 4 dpi and stained for gB. The images show a representative cell and the localization pattern
1112 of the cellular MVB marker CD63 in relation to the viral glycoproteins gB and gM. CD63 localizes
1113 to large vesicles positive for gB and gM. Scale bars indicate 10 μm. The green line indicates the
1114 section quantified in S5B. **S5B** Line plot for the indicated areas in S5A. CD63 signal correlates with
1115 gM and gB signals in two MVIBs. **S5C** Spatial weighted colocalization analysis highlights the
1116 specific areas for CD63 and gB colocalization. Scale bar indicates 10 μm.

1117

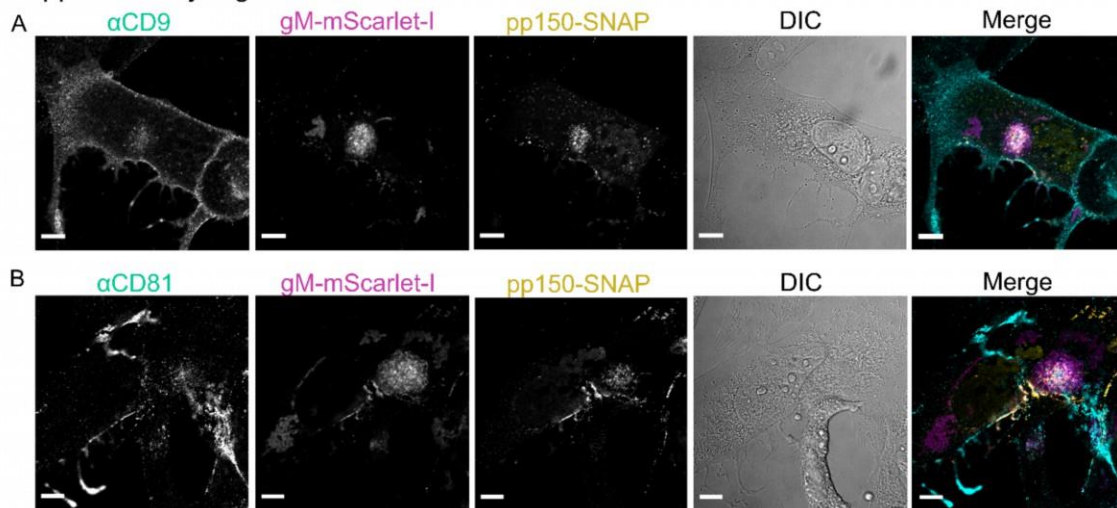
Supplementary Figure 6



1118

1119 **Supplementary Figure 6. Pathway analysis of virion mass spectrometry.** Pathway analysis
1120 of the mass spectrometry data from purified virions, done with string-db.org. The color of the dots
1121 indicates factors from either GO-term associated pathways or publications related to their
1122 functionality. The colors of the connections indicate the type of evidence for the interactions and
1123 are filtered for the highest interaction confidence (0.900) as provided by the database.

Supplementary Figure 7

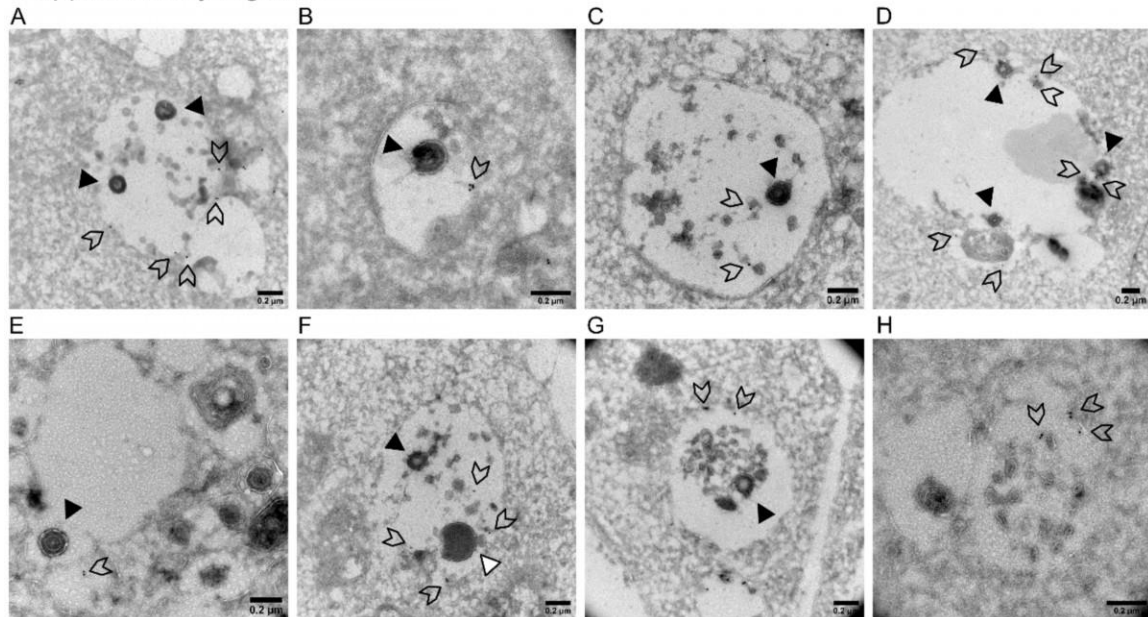


1124

1125 **Supplementary Figure 7. Tetraspanins CD9 and CD81 localize to the assembly compartment**
1126 **but not MVIBs. S7A-B** HFF cells were infected at an MOI of 1 with HCMV-pp150-SNAP-gM-
1127 mScarlet-I. Cells were fixed at 4 dpi and stained with specific antibodies for CD9 (α CD9) and CD81
1128 (α CD81). The images show representative cells and the localization pattern of the CD molecules
1129 relative to gM (gM-mScarlet-I) and pp150 (pp150-SNAP). Scale bars indicate 10 μ m.

1130

Supplementary Figure 8



1131

1132 **Supplementary Figure 8. Virus products localize to large vesicles positive for CD63.** HFF
1133 cells were infected with HCMV-TB40-WT at an MOI of 0.5. After 4 dpi, the cells were fixed and
1134 processed for immunogold labeling against CD63. Note that membranes appear white in this
1135 preparation method, and low GA concentrations used to preserve epitopes might lead to less
1136 preservation of MViB contents. **S8A-G** Shown is large bodies containing virus particles (black
1137 triangles), dense bodies (white-filled triangles), and 10 nm gold particles (arrowheads). **S8H** A
1138 body with the classical phenotype of an MVB decorated with 10 nm gold particles (arrowheads). All scale
1139 bars indicate 0.2 μm.

1140

Supplementary Figure 9

Cell middle

pp150-SNAP

gM-mScarlet-I

Merge

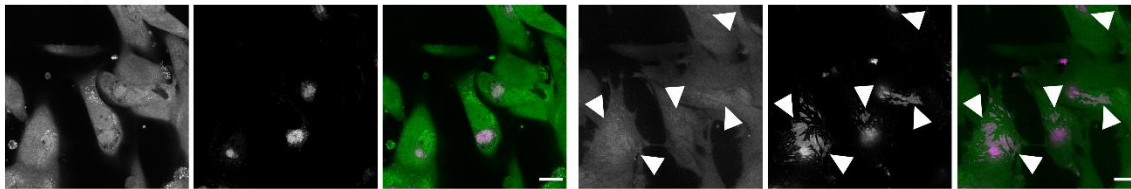
Lower plasma membrane

pp150-SNAP

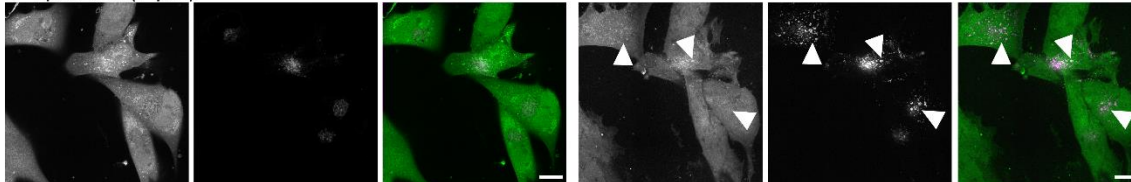
gM-mScarlet-I

Merge

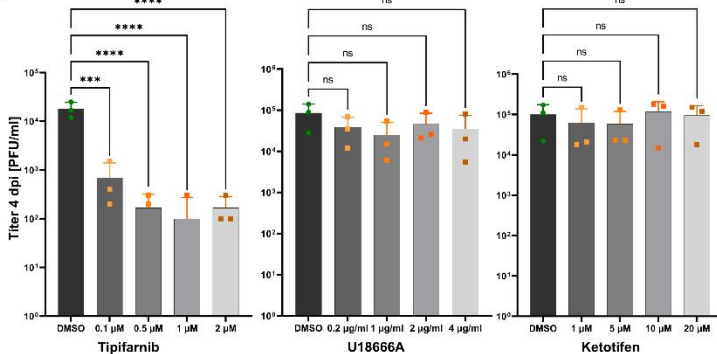
A DMSO 1:5000



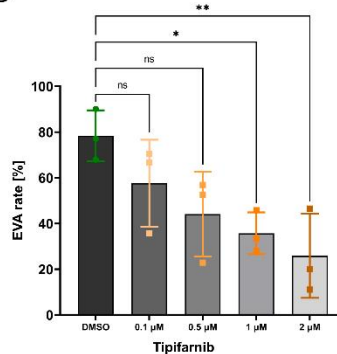
B Tipifarnib (1 μM)



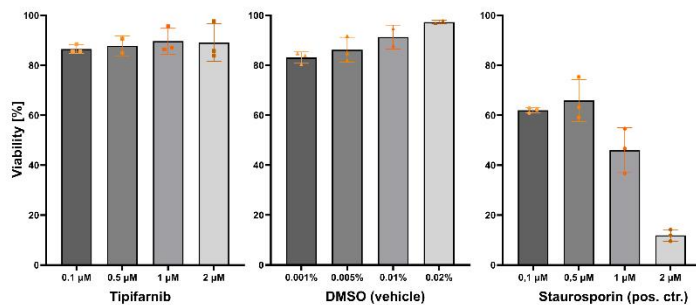
C



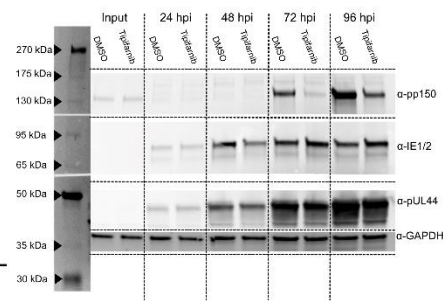
D



E



F



1141

1142 **Supplementary Figure 9. S9A-B** HFF cells were infected with HCMV-TB40-pp150-SNAP-gM-
 1143 mScarlet-I at an MOI of 2 and treated with the indicated substance at the indicated concentrations
 1144 until 5 dpi. The medium containing the inhibitors was refreshed every 24 hours. 5 dpi cells were
 1145 fixed, labeled with SNAP-Cell-SiR, and imaged by spinning-disk microscopy. White triangles
 1146 indicate EVAs. Scale bars indicate 20 μm. **S9C** HFF cells were infected with HCMV-TB40-pp150-
 1147 SNAP-gM-mScarlet-I at an MOI of 2 and treated with the indicated inhibitors at the indicated
 1148 concentrations until 4 dpi. The medium containing the inhibitors was refreshed every 24 hours. At
 1149 4 dpi, the supernatant was collected and titrated on HFF cells. Bars show mean, and error bars
 1150 indicate standard deviation. Statistical significance was probed using one-way ANOVA (p-values:
 1151 Tipifarnib: <0.0001, U18666A: 0.4154, Ketotifen: 0.8364) and Dunnet's multiple comparisons tests
 1152 (shown in the figure). **S9D** HFF cells were treated as described for S9 A-B. Large overviews were

1153 created by spinning-disk microscopy, and EVAs were quantified. Bars show mean, and error bars
1154 indicate standard deviation. Statistical significance was calculated using a one-way ANOVA ($p =$
1155 0.0179 ; in total, 687 late infected cells from triplicates were counted) and Dunnet's multiple
1156 comparisons test (shown in the figure). **S9E** HFF were treated with the indicated substance at the
1157 indicated concentration for 24 hours. Cell viability was measured with an ATP assay at 24 hpi. The
1158 apoptosis inducer Staurosporine was used as a positive control. Bars show mean, and error bars
1159 indicate standard deviation. Statistical analysis by a 2-way ANOVA confirmed statistically
1160 significant differences in the viabilities of the three groups (p -value < 0.0001). The cytotoxicity of
1161 Tipifarnib was not significantly different from the vehicle control, as determined by Tukey's multiple
1162 comparisons test. In contrast, the change in cell viability of Staurosporin was significant in the same
1163 analysis. **S9F** Western blot of HFF cells infected with HCMV-TB40-WT (MOI = 3) and treated with
1164 $1 \mu\text{M}$ Tipifarnib or DMSO (0.01%; vehicle control). At each indicated time point (input = 1 hpi), the
1165 cells were harvested and lysed, and the blot was probed for pp150 as a late protein, IE1/2 as
1166 immediate-early gene products, or UL44 as an early gene. GAPDH served as the loading control.

1167

1168 **Supplementary Video 1. SBF-SEM of an area between the cell surface and the growth**
1169 **substrate.** The video shows a subset of planes from the dataset described in Fig. 1 rendered as a
1170 video. Infection conditions are as described before. The signal was inverted to resemble TEM
1171 contrast. Shown is a large invagination below the cell at the growth substrate.

1172 **Supplementary Video 2. 3D-rendering of an MViB from SBF-SEM data.** In this video an MViB
1173 from the SBF-SEM dataset described in Fig. 2 is rendered in 3D. The yellow surface marks the
1174 limiting membrane of the multivesicular structures. The contents are rendered as surfaces in
1175 different colors to show the heterogeneity of the MViB cargo. Virions are rendered in dark green,
1176 dense bodies in cyan, and other vesicular material in magenta. Scale bar indicates 600 nm.

1177

1178 **Supplementary Videos 3A and 3B. SBF-SEM rendering of infected HFF cells.** The video shows
1179 an excerpt from the dataset described in Fig. 1. HFF cells were infected with an MOI of 3 and fixed
1180 4dpi. **3A** Overview rendering of the whole SBF-SEM dataset of the cells shown in Fig. 1 and 2. **3B**
1181 A group of prominent virus-filled MVBs is highlighted by a surface rendering. Several more MVBs
1182 are present in the cell.

1183

1184 **Supplementary Video 4. Stack of an MViB and associated immature particles.** This video
1185 shows an MViB from the SBF-SEM dataset shown in Fig. 1. Cells were infected and treated as
1186 described before. White triangles indicate immature, non-enveloped particles in close proximity or
1187 directly associated with the multivesicular structure next to the nucleus. Scale bar indicates 0.2 μm .

1188 **Supplementary Video 5. Multi-perspective 3D rendering of volumetric time-lapse**
1189 **microscopy data of HCMV release.** HFF cell, infected with HCMV-pp150-EGFP-gM-mCherry as
1190 described in Fig. 3A. The video shows several perspectives on how a large MViB positive for pp150-
1191 EGFP (green) and gM-mCherry (red) traverses the cytoplasm and fuses with the plasma
1192 membrane. The first seconds show the 3D video, followed by a split-screen part of three different
1193 perspectives. A spotlight effect (circle) highlights the same body in all three parts. In the left third,
1194 the MViB is followed by a moving section parallel to the growth substrate, through the volume on
1195 its way downwards to the lower cell surface. In the middle part, the body is followed as a 3D
1196 rendering through the cell. The camera angle moves to keep the body visible as well as possible.
1197 The last third shows how the MViB fuses with the plasma membrane in a static cross-section. Due
1198 to the optical setup of the lattice-light-sheet microscope (See Fig. 3A), the grid added by Arivis 4D
1199 (Arivis AG, Rostock, Germany) is tilted 30° respective to the real physical orientation of the cell in
1200 the microscope.

1201 **Supplementary Videos 6 and 7. Live-cell long time-lapse spinning-disk microscopy videos.**
1202 HFF cells were infected with HCMV-pp150-SNAP-gM-mScarlet-I at an MOI of 1. At 72 hpi, cells
1203 were stained for pp150-SNAP and imaged live by spinning-disk microscopy. 8-micrometer stacks
1204 in 1-micrometer increments were acquired every 40 minutes. The plane shown is the section of the
1205 cell closest to the coverglass. Cells can be seen to release virus particles in short intermittent bursts
1206 over several hours, indicated by the white arrowheads. pp150-SNAP labeling is shown in green
1207 and gM-mScarlet-I label in magenta. The time format is hh:mm.

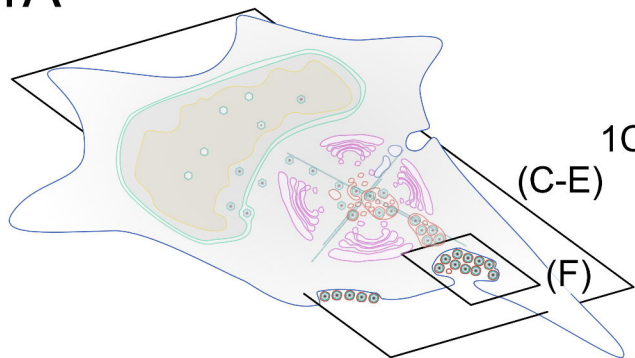
1208

1209 **Supplementary Video 8. 3D rendering of immunofluorescence data.** In this video, the IF
1210 dataset from Sup. Fig. 6 is rendered in 3D. The coloring scheme is the same as in Sup. Fig. 6.
1211 The 3D rendering shows the 3-dimensional correlation between the molecules.

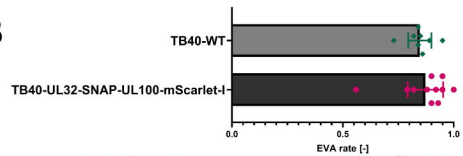
1212

1213 **Supplementary Table 1** Mass Spectrometry Results

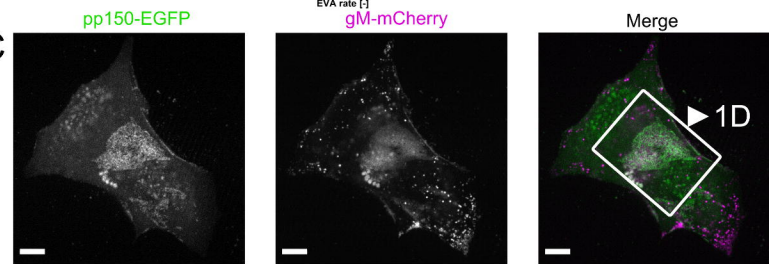
1A



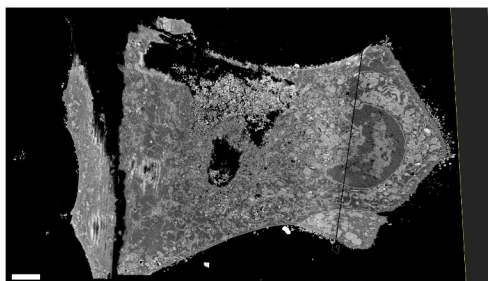
1B



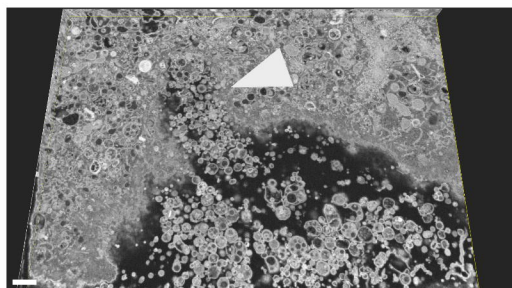
1C



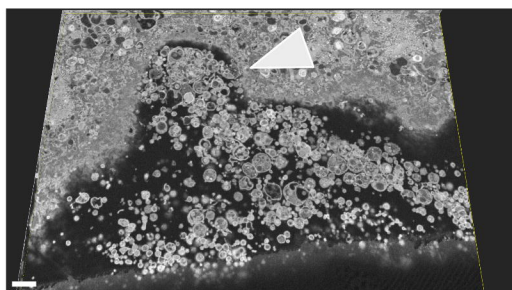
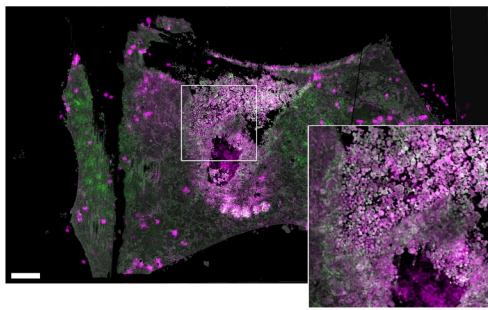
1D

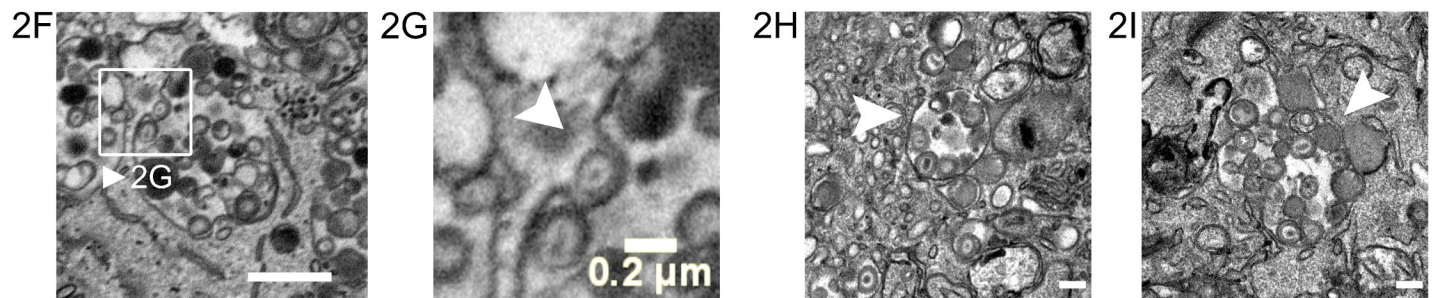
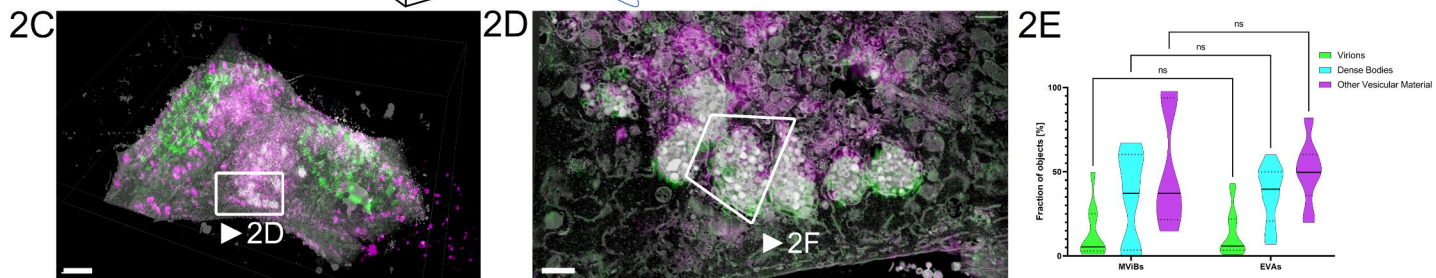
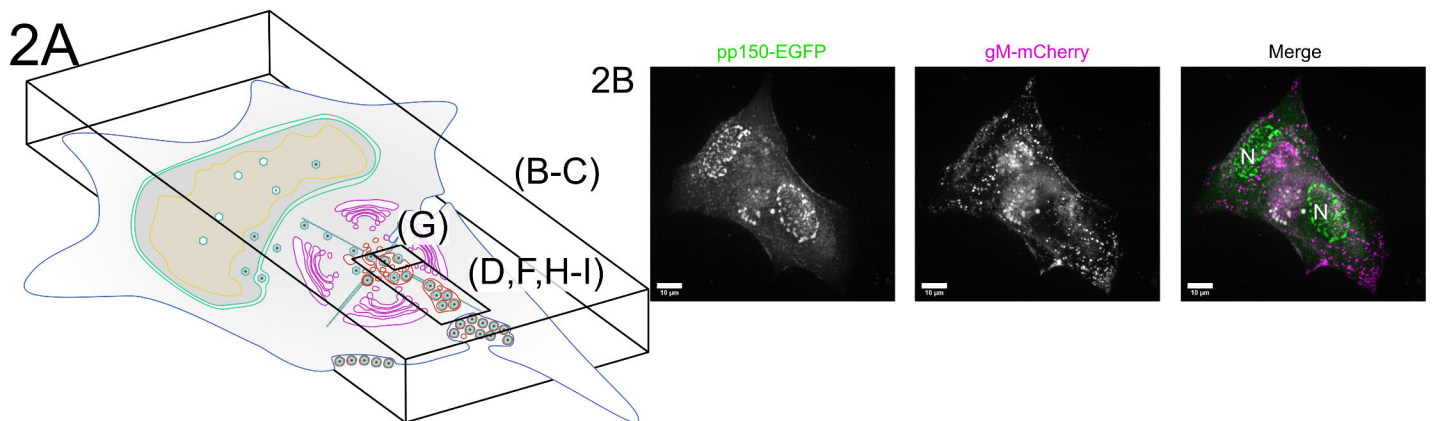


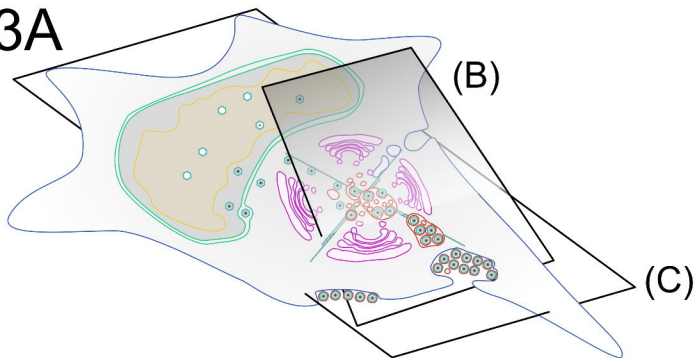
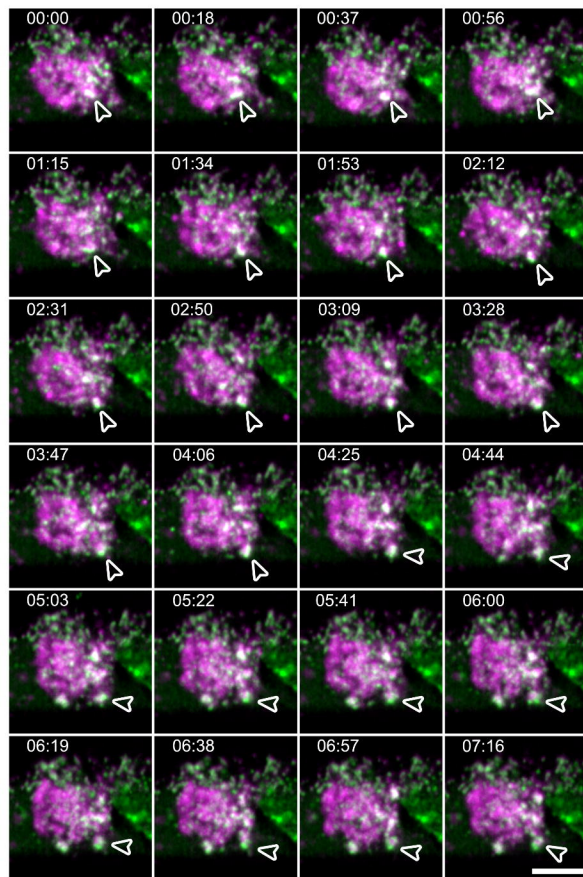
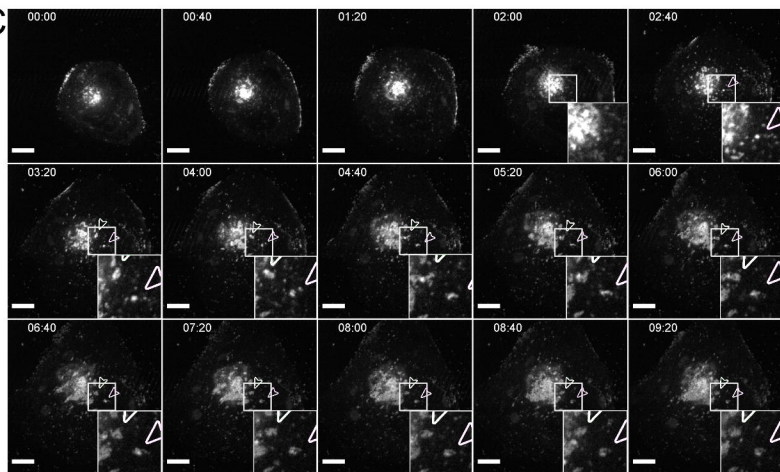
1F



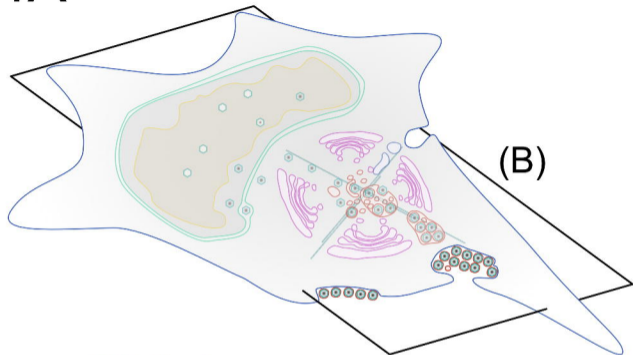
1E



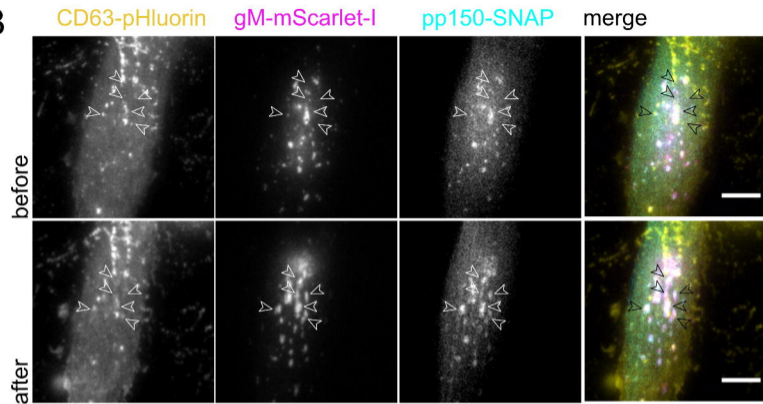


3A**3B****3C**

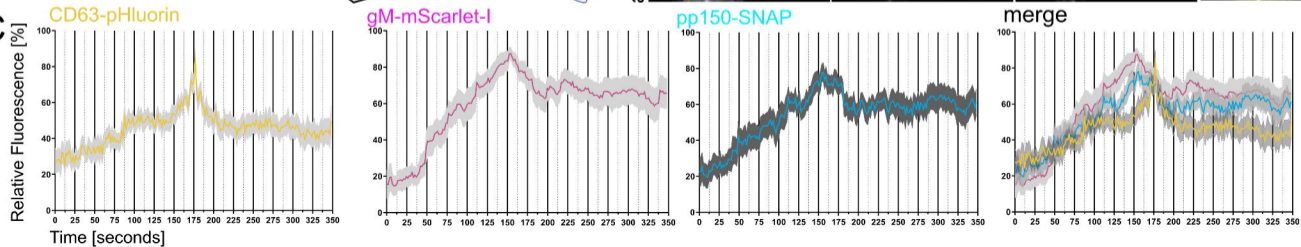
4A

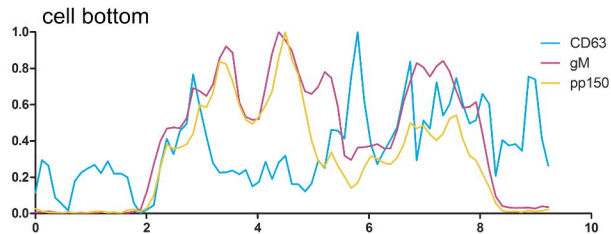
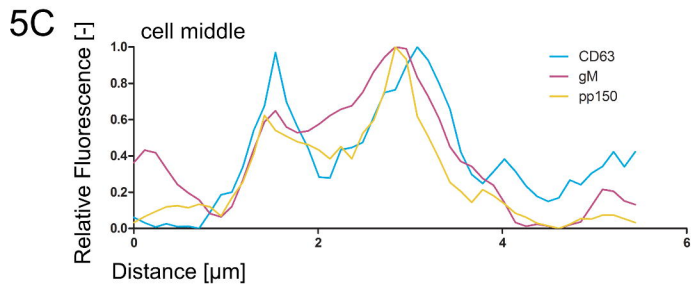
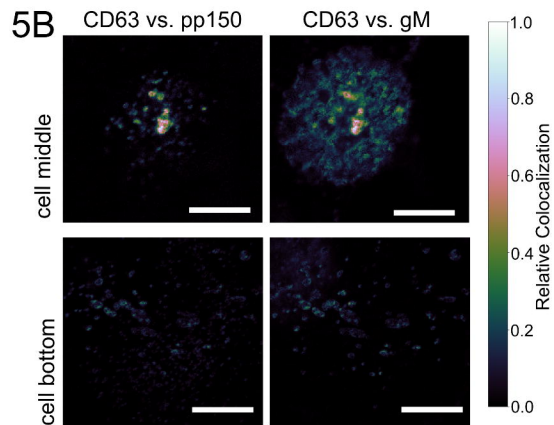
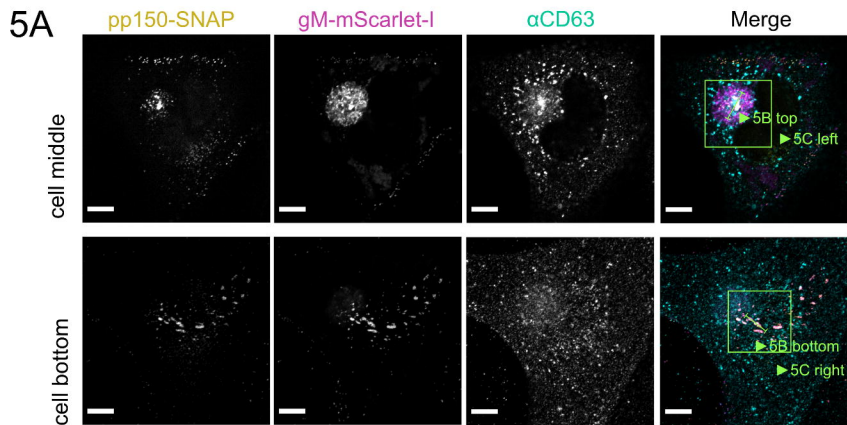


4B



4C





6

